

The climate of Mars from assimilations of

Mars Climate Sounder data

DPhil 1st Year Report

Tao Ruan

Atmospheric, Oceanic and Planetary Physics

(AOPP)

Department of Physics

Lincoln College

University of Oxford

Supervisors

Professor Peter Read (University of Oxford)

Dr. Stephen Lewis (The Open University)

Word Count: 14379

Acknowledgements

I would like to express my gratitude to both of my supervisors Prof. Peter Read and Dr. Stephen Lewis for their priceless advice and idea, the codes they share with me, and especially for their understanding of my personal circumstance.

Besides I also want to thank M. D. Smith, NASA-Goddard Space Flight Center for providing the MGS/TES observations and Dr. Luca Montabone for preparing the data for data assimilation tests and the assimilation results analyzed in the Chapter 3.

Abstract

The works carried out during the first year of my DPhil project are presented in this report. The objective of this project is to make use of a unique and advanced data assimilation system that enables the combining of observational data with predictions from a global numerical model of the Martian atmospheric circulation. In this report, an introduction to the planet Mars and a brief description of observations used in this project will be included, as well as an overview of modeling works conducted in Oxford and by other groups, mainly on dust-related topics. Following the introduction, we present a brief description of the Martian General Circulation Model (MGCM) employed in this project. A new data assimilation approach will be developed based on the MGCM described in this report. A study of semi-annual oscillations on Mars from diagnostics of the assimilation results of Montabone et al. [2005] will be presented as well. A clear signature of semi-annual oscillations is observed in the assimilation results, and detailed analysis by Singular Spectrum Analysis (SSA) also gives us a better understanding of this semi-annual cycle. Meanwhile, the first attempt to develop an advanced data assimilation technique that includes a full assimilation of 3-D dust measurements into a model that represents the full dust transport cycle is also an important aim of this report. The progress achieved so far on the latest 2-D dust data assimilation scheme with dust transport is encouraging for the development of future 3-D dust data assimilation scheme with dust transport. Finally, the future plan of this ongoing project is also discussed in the concluding chapter.

Contents

Chapter 1 Introduction.....	1
1.1 Background	1
1.2 Observation.....	6
1.2.1 TES.....	6
1.2.2 MCS	9
1.3 Modeling studies.....	10
1.4 Motivation and objectives	15
Chapter 2 Martian General Circulation Model	19
2.1 Model Dynamics	19
2.2 Surface Processes.....	21
2.3 Subgrid Dynamics.....	21
2.4 Dust lifting mechanisms.....	22
2.4.1 Dust lifting by near-surface wind stress.....	22
2.4.2 Dust lifting by the activity of dust devils.....	23
2.5 Data assimilation.....	23
Chapter 3 Interannual and Interseasonal Variability of Martian Climate using Data Assimilation: A Semi-Annual Oscillation	27
3.1 Previous work of semi-annual oscillation on Mars.....	27
3.2 Study of semi-annual oscillation with our MGCM.....	29
Chapter 4 2-D Data Assimilation of Column Dust Opacity with Dust Transport.....	38
4.1 Background of the application of data assimilation on Mars	38
4.2 Approach of 2-D dust data assimilation with dust transport.....	39
4.3 Preliminary results	40
Chapter 5 Conclusions and Future Plans	45
5.1 Conclusions	45
5.2 Future Work	46
5.3 Expected Timetable	48
Bibliography	50

Chapter 1 Introduction

1.1 Background

The most famous events reminding people of Mars in the last century were probably the Viking missions of the 1970s and 1980s. In spite of the failure of the Mars Observer mission in 1993, and the loss of both the Mars Climate Orbiter and Mars Polar Lander spacecraft in 1999, which were significant setbacks to the research aspects of Mars [Euler et al., 2001], it is lucky that our passion of exploring the other planets in our solar system is still thriving. A series of instruments on different missions have been working in their orbits to provide relatively complete observational datasets for Martian researches. For instance, Mars Global Surveyor / Mars Orbiter Camera (MOC), Mars Global Surveyor / Thermal Emission Spectrometer (TES), Mars Odyssey/Thermal Emission Imaging System (THEMIS), Mars Reconnaissance Orbiter / Mars Climate Sounder (MCS) and so forth. Apart from the research aspects of observations, plenty of modelling studies have been conducted using different models developed in different institutions [Forget et al., 1999; Basu et al. 2004; Montabone et al., 2005; Lewis et al., 2005; Lewis et al., 2005; Wilson et al., 2008; Kuroda et al., 2008;].

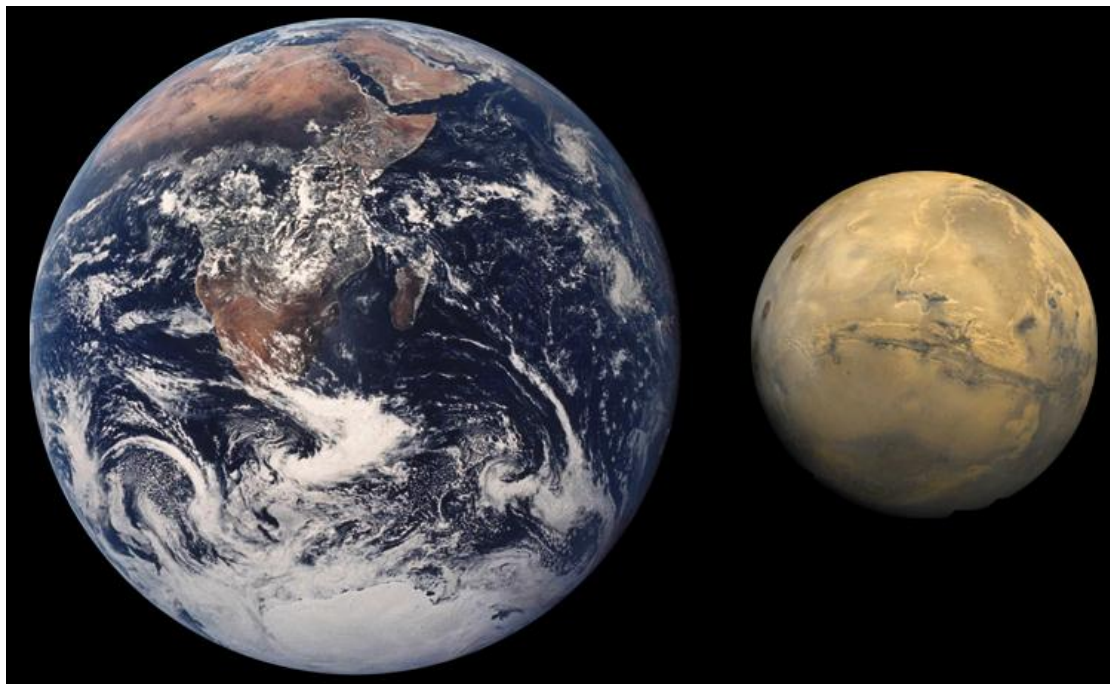


Figure 1.1. comparison of the sizes of the Earth and the Mars (from wikipedia).

Most people are likely to be more familiar with the Earth than with Mars, so it is better to start to describe some main characteristics of Mars as a planet along with the Earth. Our nearest neighbour, Mars, is a rocky body with half the size of earth (Figure 1.1) and at a comparable distance to the sun (1.38 – 1.67 AU) compared to that of the Earth (0.98 – 1.02 AU). The rotation period around its axis is approximately 40 mins longer than the length of day on Earth and the planetary obliquities of both planets are close to each other at the present time (25.19° for Mars while 23.93° for the Earth). It implies that their tropics are heated by the sun stronger than the polar area and the seasonal variations can be observed in both planets in the light of the rotation about the Sun. But the year length on Mars is nearly 100% longer than that of Earth, (668 days compared to 365 days), which results from Mars's greater distance from the Sun. The surface gravity on Mars is around one third ($3.72 m \cdot s^{-2}$) of the Earth's ($9.81 m \cdot s^{-2}$). It seems that in both planets the atmospheric circulation prefers to transport heat from the equator to the high latitudes, and the coriolis force has a similar effect on the atmospheric motions. This results in the development of baroclinic instabilities at mid-latitudes and probably the similar phenomenon of wave propagation. The much more elliptical orbit of Mars leads to some significant asymmetries between the seasons in the two hemispheres compared to the Earth. The details of the parameters for both planets are shown in Table 1.1.

	Earth	Mars
Mean orbital radius (10^{11} m)	1.50	2.28
Distance from Sun (AU)	0.98-1.02	1.38-1.67
Orbital eccentricity	0.017	0.093
L_s of perihelion	281°	251°
Planetary obliquity	23.93°	25.19°
Rotation rate, Ω ($10^{-5} s^{-1}$)	7.294	7.088
Solar day, sol (s)	86,400	88,775
Year length (sol)	365.24	686.6
Year length (Earth days)	365.24	686.98
Equatorial radius (10^6 m)	6.378	3.396
Surface gravity, g (ms^{-2})	9.81	3.72
Surface pressure (Pa)	101,300	600(variable)
Atmospheric constituents (molar)	N_2 (77%)	CO_2 (95%)

ratio)

	O ₂ (21%)	N ₂ (2.7%)
	H ₂ O(1%)	Ar(1.6%)
	Ar(0.9%)	O ₂ (0.13%)
Gas constant, R(m ² s ⁻² K ⁻¹)	287	192
c _p /R	3.5	4.4
Mean Solar Constant (Wm ⁻²)	1367	589
Bond Albedo	0.306	0.25
Equilibrium temperature, T _e (K)	256	210
Scale height, H _p =RT _e /g (km)	7.5	10.8
Surface temperature (K)	230-315	140-300
Dry adiabatic lapse rate (K km ⁻¹)	9.8	4.5
Buoyancy frequency, N(10 ⁻² s ⁻¹)	1.1	0.6
Deformation radius, $L = NH_p/\Omega$	1100	920
(km)		

Table 1.1, Parameters in the Earth and Mars (adapted from Read & Lewis (2004)).

Compared to the Earth, the Martian atmosphere is thin and composed mainly of CO₂ with small amounts of nitrogen (N₂), argon (Ar) and very little oxygen (O₂). The total pressure of atmosphere on Mars is only 0.5%-1% that of the Earth. On Earth, the water vapour makes the 1% of the atmospheric mass, while the concentrations of water vapour is measured in precipitable microns, which means if all the water contained in a vertical column of atmosphere were condensed to a liquid state, it would form a layer typically only a few microns thick. Therefore, the Martian atmosphere has very low absolute humidity. Actually, because of the low mean pressure of the Martian atmosphere, close to that of the triple point of water, ice could not melt into liquid water in most places but would sublime directly into water vapor regardless of temperature below the normal freezing point of water (i.e., around 273 K at 1 bar). These lead to a very dry climate on Mars. It is obvious that a desert-like landscape can be found easily in regions outside the polar areas. One image of the Martian surface captured by the Viking Lander (VL) spacecraft is shown in Figure 1.2.

Various landscapes can be found on Mars, including extensive sand-covered deserts in the northern tropics, mid latitudes to arctic ice-fields, mountainous terrain and so on. Each landscape has its own characteristic local weather in terms of wind patterns,

temperature and occasional clouds.

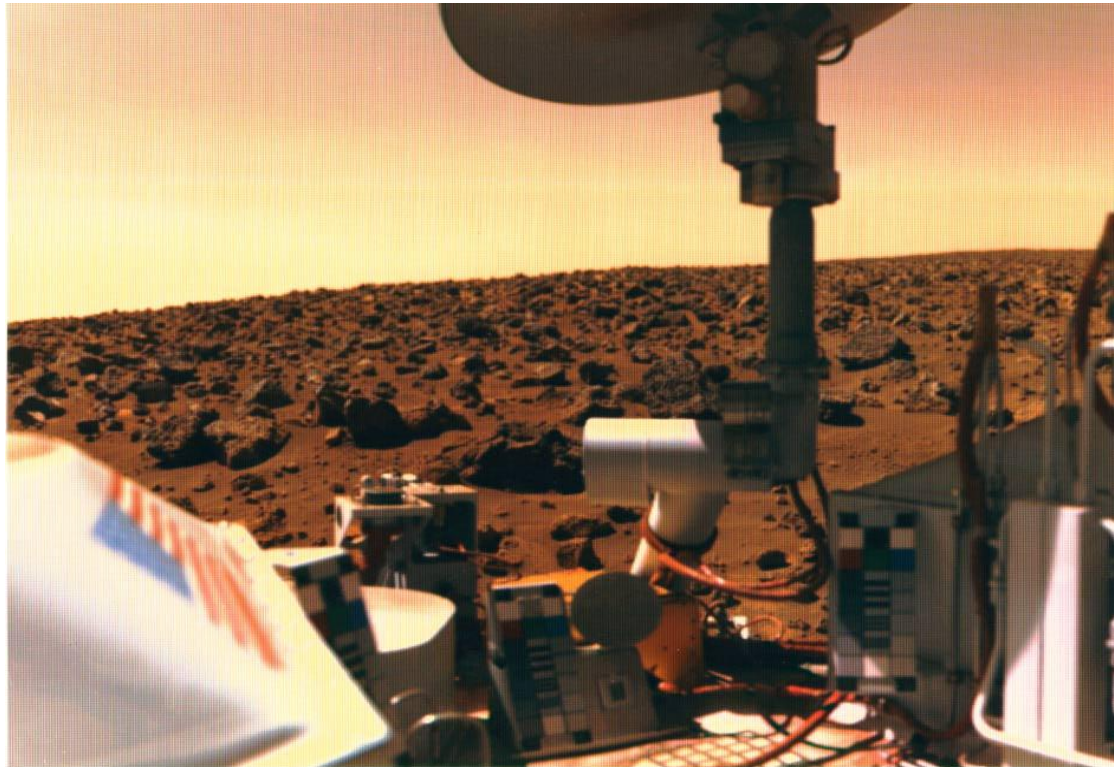


Figure 1.2 Viking Lander view of the Martian Surface (from <http://mars.jpl.nasa.gov>)

Apart from some similarities between Mars and Earth, dust is an extremely important property on Mars. Martian atmospheric dust itself can strongly emit the radiation in the infrared after absorbing short-wave solar radiation and also has great capability of absorbing the long-wave surface radiation [Newman et al., 2002a]. Besides, there is a potential to develop dust storm on Mars locally and globally. Dust particles can be lifted by near-surface wind stress and dust devils [Newman et al., 2002a] so that some more dust can get into the dust cycle, and can settle back on the Martian surface by the sedimentation mechanism. Thus, Martian dust has a considerable impact on the thermal and dynamical state of the atmosphere.

The classification of dust storms in the report produced by Montabone et al. [2010] will be described here. According to the classification based on a size-duration relationship [Cantor et al., 2001], the types of dust storm can fall into three categories, local dust storms, regional storms and planetary-encircling storms. The local dust storm is defined by the size of the affected area lying between 10^2 km^2 and $1.6 \times 10^6 \text{ km}^2$ and a duration of less than 3 days (one of the local dust storms captured by the camera onboard the Viking Orbiter 2 is shown in Figure 1.3). The term 'regional dust storm' is applies when the size of the affected area is larger than $1.6 \times 10^6 \text{ km}^2$ and of

duration more than 3 days (an image of a regional dust storm from Viking Orbiter 2 is shown in Figure 1.4). The planet-encircling dust storm refers to those multi-regional storm events which spread dust in the atmosphere across most longitudes. Thus they will have effects at global scale and a last long time until most dust settles by going into the global dust transport cycle or dropping back to the Martian surface (images from MGS/Mars Orbiter Camera are shown in Figure 1.5).

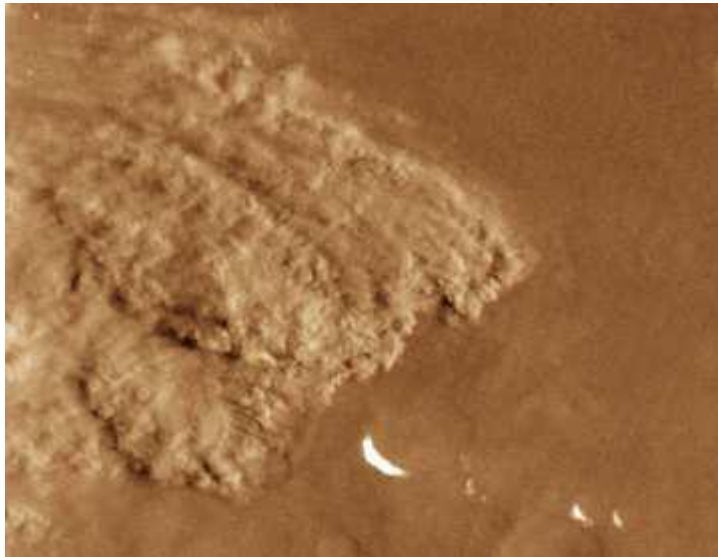


Figure 1.3. Local dust storm near the edge of Mars's shrinking south polar cap in a picture taken by the Viking Orbiter 2. Credits to NASA/JPL. (from the report produced by Montabone et al., 2010)

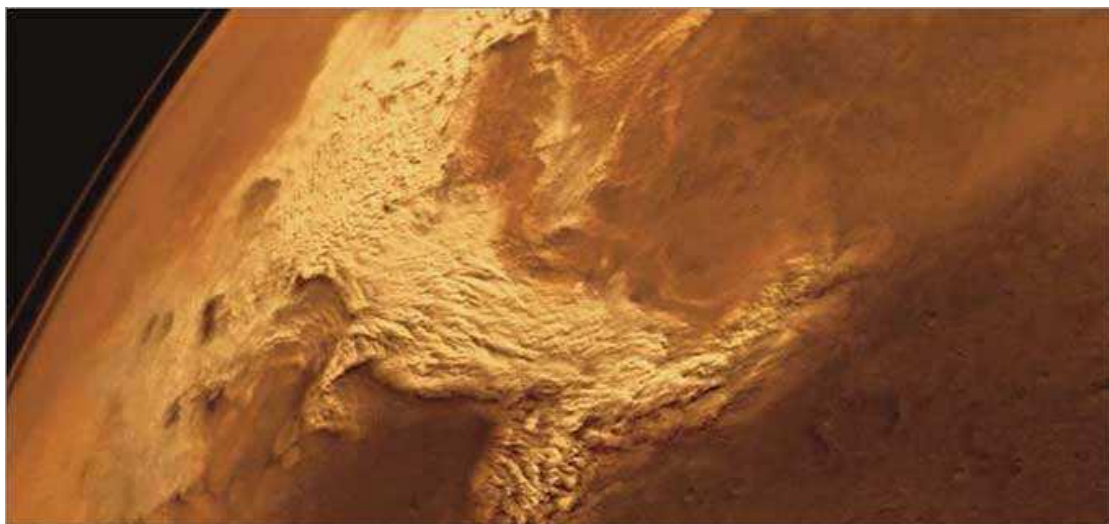


Figure 1.4. Regional dust storm in Thaumasia (40°S, 90°W). Image from Viking Orbiter 2, 17 February 1977 ($L_s = 205.5^\circ$). Credits to NASA/JPL. (from the report produced by Montabone et al., 2010)

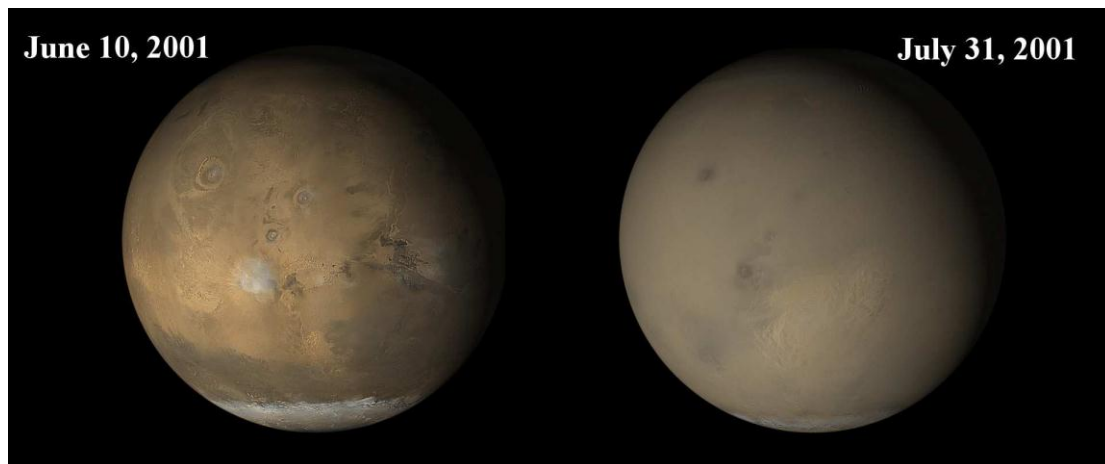


Figure 1.5. MGS/Mars Orbiter Camera pictures of Mars before (10th June 2001) and during (31st July 2001) the planet-encircling dust storm of Martian year 25 ($L_s \vee 186^\circ$). The global views of Mars are centred on the Tharsis Plateau. (from the report produced by Montabone et al., 2010)

1.2 Observations

Observations not only contribute to the understanding of Martian atmosphere directly, but also are important inputs for model studies, especially for the data assimilation. As the objective of my DPhil project concerns about data assimilation in terms of technique aspect, it is necessary to address the main observations involved in this project.

1.2.1 TES

A lack of complete sets of observational data significantly impedes the detailed study of the Martian atmosphere. The operational mapping of Martian atmospheric properties by the Mars Global Surveyor (MGS) spacecraft started work on 1 March 1999 ($L_s = 104^\circ$). The details can be found in the work of Smith [2004]. The retrievals from the infrared spectra returned by the on-board Thermal Emission Spectrometer (TES) are capable of providing detailed information on atmospheric and surface temperature, dust and water ice aerosol optical depth, and water vapor column abundance.

MGS is in a Sun-synchronous, nearly polar orbit. The atmospheric retrievals are based on 3x2 pixels of each TES footprint, and the corresponding spatial resolution is 9 km in the east-west direction and 10-20 km in the north-south direction by

considering the impact of spacecraft motion. MGS provides two sets of twelve such strips-like datasets each day, one of which set is taken near a local time of 1400 hours and the other of which is taken near a local time of 0200 hours. A constrained linear inversion of radiance in the $15\text{-}\mu\text{m}$ CO_2 band [Conrath et al., 2000] is used to retrieve atmospheric temperature as a function of pressure. The uncertainty of temperatures is $\sim 2\text{K}$ in the middle atmosphere ($\sim 10\text{-}30\text{km}$), and larger both in the lowest scale height and at the highest altitudes where limb observation are used [Smith, 2004].

After completing the retrieval of atmosphere temperature, the TES data team starts to retrieve aerosol optical depth in a separate second step. The retrieval algorithm is mainly based on the method used for Mars Odyssey THEMIS infrared data but with further improvements [Smith, 2004]. The values of surface temperature, dust and water ice optical depth which provide the best fit between computed and observed radiance is the key output of the retrieval algorithm for aerosol optical depth. The

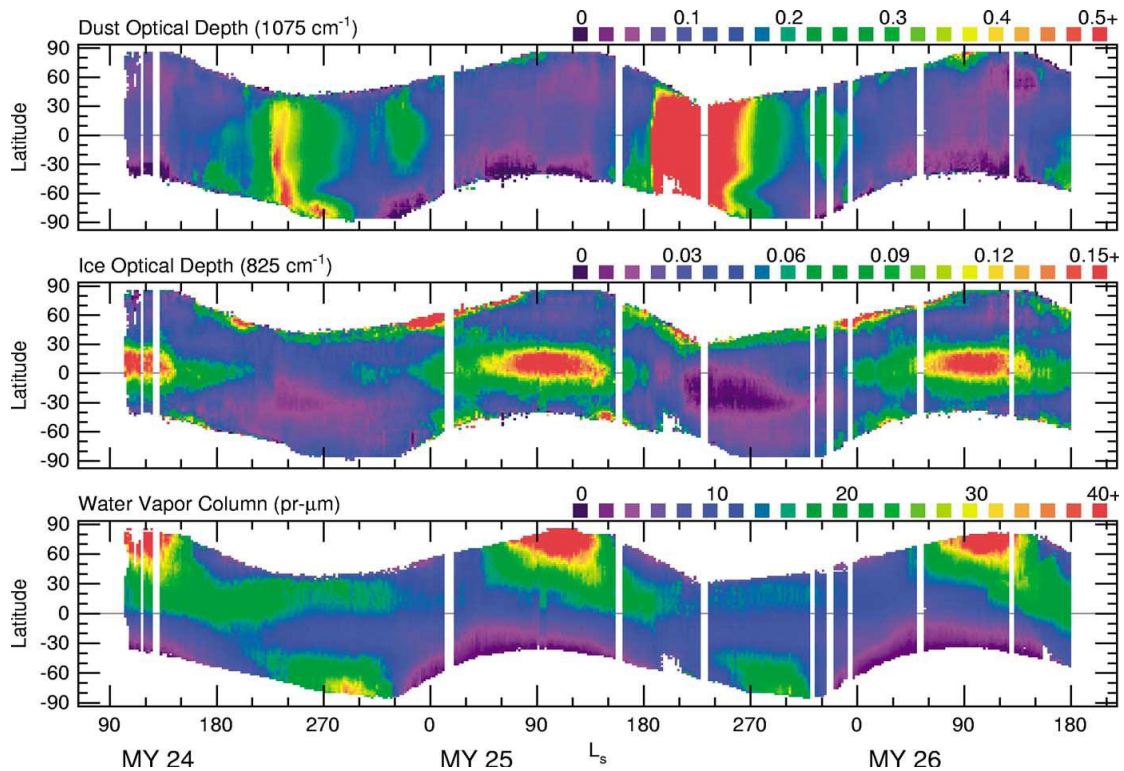


Fig. 1.6. An overview of TES daytime (local time ~ 1400) aerosol optical depth and water vapor abundance. Shown is the zonal average of each quantity a function of latitude and season (L_s). (Top) Dust optical depth at 1075 cm^{-1} scaled to an equivalent 6.1 mbar pressure surface (to remove the effect of topography). (Middle) Water ice optical depth at 825 cm^{-1} . (Bottom) Water vapor column abundance in precipitable microns ($\text{pr-}\mu\text{m}$). The largest data gaps were caused by solar conjunction and various times when the MGS spacecraft went into

contingency (safing) mode.(from the work of Smith, 2004).

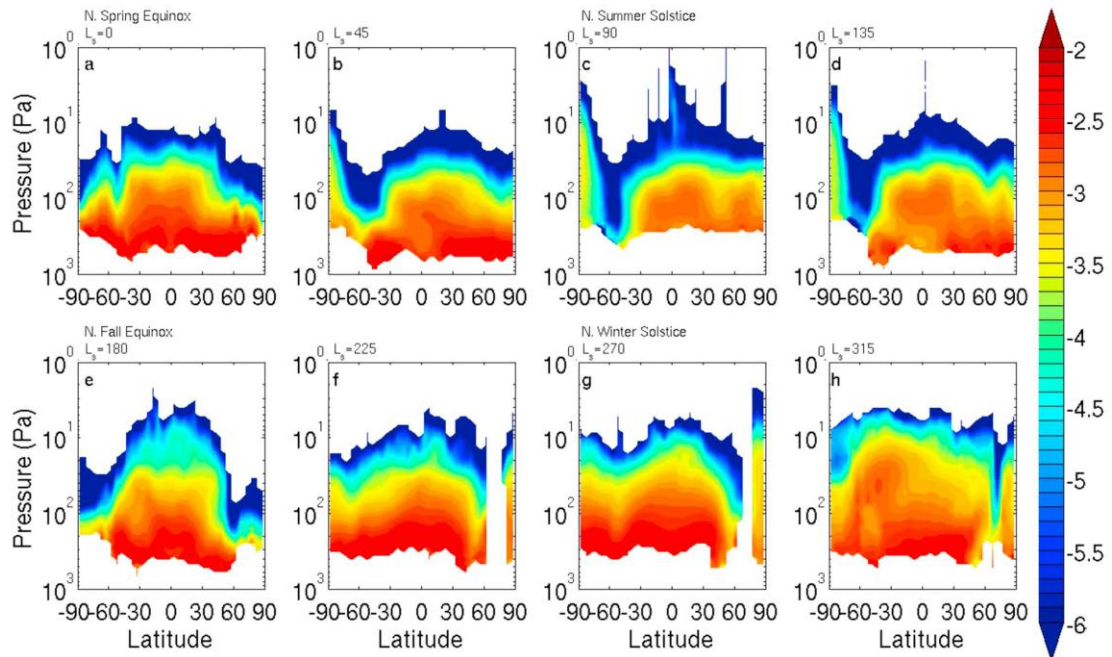


Figure 1.7. Log10 of the zonal average dust opacity (km^{-1}) nightside retrievals of MY 29 for the Ls bins labeled at the top of each panel. Contours are shown every 0.1 log units. Note the pressure scale is between 1000 and 1 Pa. (from the work of McCleese et al., 2010).

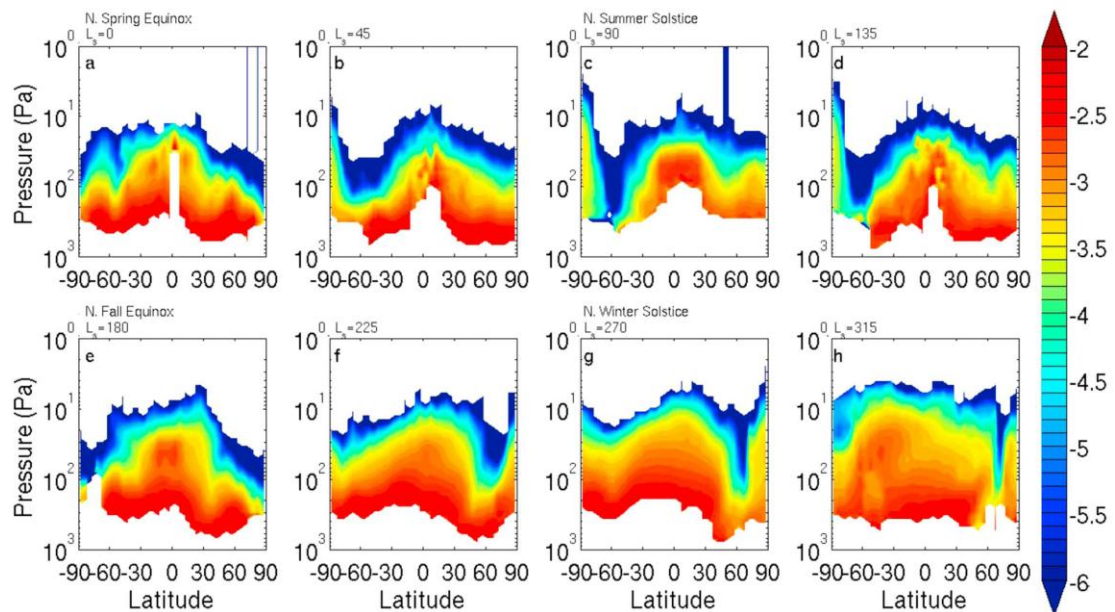


Figure 1.8. Log10 of the zonal average dust opacity (km^{-1}) dayside retrievals of MY 29 for the Ls bins labeled at the top of each panel. Contours are shown every 0.1 log units. Note the pressure scale is between 1000 and 1 Pa. (from the work of McCleese et al., 2010).

detail of the algorithm was described in the work of Smith [2004]. An overview of the retrievals of dust and water ice optical depth, and water vapor column abundance is shown in Figure 1.6 in terms of the analysis of Smith [2004]. The values shown in Figure 1.6 are the zonal means of day-time (local time ~ 1400 hours) measurements as a function of solar latitude (L_s) and latitude. In order to obtain adequate thermal contrast between the surface and the atmosphere, the retrieval algorithm is restricted to inverting those spectra with a surface temperature greater than 220K.

1.2.2 MCS

The Martian Climate Sounder (MCS) instrument is now operational onboard on the Mars Reconnaissance Orbiter (MRO) [McCleese et al., 2007]. The aim of MCS is to measure the Martian surface and atmosphere using limb, nadir and off-nadir viewing geometries. The data started being taken by MCS on 24 September 2006 ($L_s = 111^\circ$). A mechanical anomaly happened between 9 February and 14 June 2007 however, the details of which can be found in the paper of Kleinbohl et al. [2009]. Pressure and vertical profiles of atmospheric temperature, dust opacity and water ice opacity can be retrieved from the MCS instruments. A series of analysis have been conducted based on these datasets, which include investigating the temperature maximum in the polar middle atmosphere during southern hemisphere winter [McCleese et al., 2008], the atmospheric thermal tides [Lee et al., 2009], seasonal variations in zonal mean temperature, dust and water ice aerosols [McCleese et al., 2010], ice and dust layering in the Martian atmosphere [Benson et al., 2011] etc.

MRO is also in a polar, sun-synchronous orbit around Mars. This orbit globally covers the day and night sides of the atmosphere, allowing diurnal and seasonal atmospheric trends to be separated. The channels used for the infrared radiometer are summarized in Table 2. The pressure can be retrieved very precisely with an uncertainty of 1%-2%, and it is frequently used as a vertical coordinate for atmospheric profiles. The retrieval of temperature profiles are over a range from 5-10 to 80-90 km altitude, and the typical vertical resolution is 4-6 km with a precision

Channel	Band Pass (cm^{-1})	NER ($\text{mWm}^{-2}\text{sr}^{-1}/\text{cm}^{-1}$)	Main Absorbers
A1	595-615	0.0557	CO_2
A2	615-645	0.0399	CO_2
A3	635-665	0.0419	CO_2

A4	820-870	0.0287	H ₂ O ice
A5	400-500	0.0278	Dust
B1	290-340	0.0453	Dust
B2	220-260	0.0568	H ₂ O vapor, H ₂ O ice
B3	230-245	0.174	H ₂ O vapor, H ₂ O ice

Table 2. Bandpasses of the MCS Infrared Channels, their Noise Equivalent Radiances for a 2-s Integration, and the Main Absorbers in the Martian Atmosphere at these frequencies (adapted from the work of Kleinbohl et al., 2009).

0.5-2 K over most of this altitude range. The profiles of dust and water ice opacity also achieve similar vertical resolution as temperature profiles, about 5 km, and their precisions are 10^{-4} - 10^{-5} km⁻¹ at 463 cm⁻¹ and 843 cm⁻¹, respectively [Kleinbohl et al., 2009].

McCleese et al. [2010] have used MCS data to analyze the structure and dynamics of the Martian lower and middle atmosphere in terms of temperature, dust, water ice and even the zonal gradient wind outside the tropics derived from zonal average temperature. In their study, McCleese et al. indicated that the Martian atmosphere has two modes: a symmetrical equinoctial structure with middle atmosphere polar warming and a solstitial structure with an intense middle atmosphere polar warming overlying a deep winter polar vortex. The zonal average dust opacity retrieved from MCS data are shown in Figures 1.7 and 1.8, respectively for nightside and dayside. It is obvious that the latitudinal vertical distribution of dust also has equinoctial and solstitial modes. For the equinoctial mode the dust penetrates to high altitudes over the tropics but a lower height of penetration can be found near the poles (Figure 1.7a). For the solstitial mode, the dust penetrates to high altitudes over the tropics, and a region of nearly dust-free air in the winter hemisphere midlatitudes could be observed clearly (Figure 1.7c). However, the quantitative aspects of these features could differ in both solstitial [McCleese et al., 2010].

1.3 Modeling studies

The comprehensive general circulation modelling of the Martian atmosphere can be traced back to the work of Leovy and Mintz [1969], in which a two-level terrestrial GCM originally developed at the University of California, Los Angeles (UCLA) was applied to study Martian wind systems, thermal structure and energetics. Atmospheric

condensation of CO₂ and the presence of transient baroclinic waves in the winter mid-latitudes were simulated by this model. From the early 1970s, further model development was conducted continually at NASA's Ames Research Center, resulting in a model known as the NASA Ames Mars GCM. With the topographic data released from Mariner 9 measurements, the NASA Ames Mars GCM started to include spatially varying surface elevation at the model's lower boundary. The first 3-D simulations of a global dust storm were conducted with the Ames Mars GCM incorporating a tracer transport scheme [Murphy et al., 1995]. The important role of dust transport by atmospheric eddies and the seasonal and topographic effects resulting in the differences in each hemisphere were illustrated in their work, as well as the Martian polar warming and the relationship between CO₂ column loading and the onset of major dust storms.

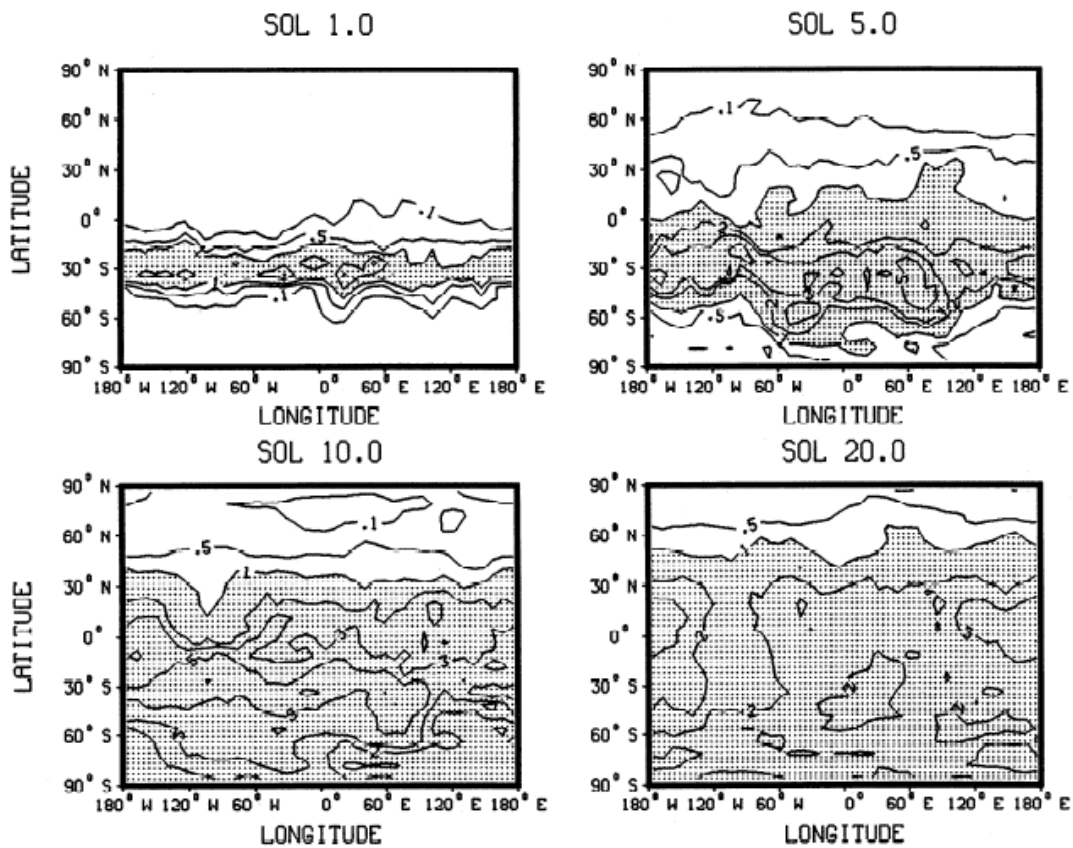


Figure 1.9. Instantaneous visible ($0.67 \mu\text{m}$ wavelength) dust opacity after sols 1, 5, 10 and 20 of the baseline simulation (zonally symmetric dust source); contours at 0.1, 0.5, 1.0, 2.0, 3.0, 5.0, 10.0. Opacities greater than unity are shaded. (from the study of Murphy et al., 1995).

The baseline simulation in the study of Murphy et al. [1995] started with a 30-sol dust-free spin-up at northern winter solstice (solar latitude $L_s = 273$). Initial surface pressure was specified in terms of altitude at each grid point, with initial global

average values of 7.6 mbar. After spin-up, the MGCM was coupled with an aerosol model (described in detail in their work) interactively. They prescribed a uniform dust source in the aerosol model on the entire surface between the 15°S and 37.5°S [Murphy et al., 1995]. The source magnitude was $1.54 \times 10^{-7} \text{ kgm}^{-2}\text{s}^{-1}$ for 10 sols with a prescribed size distribution and a particle material density of 3000 kg m^{-3} [Toon et al., 1977]. The simulation was conducted for an additional 40 sols after steady dust injection for 10 sols. In their baseline simulation (see Figure 1.9), the dust spread all over the domain except the northern polar region at a rapid pace (by 20 sols, see Figure 1.9d). The $\tau_{vis} = 1$ line moves to 10°N by sol 5 (Figure 1.9a), then to about 40°N by sol 10. By sol 20 (Figure 1.9d), the dust had reached 50°N and the spread of dust was much faster moving to the south from the original dust source region prescribed in this study. The optical depth higher than $\tau_{vis} = 1$ line could almost cover the southern hemisphere by sol 20 (Figure 1.9d). The dust distribution developed very asymmetrically within the south of the dust input corridor (Figure 1.9b, c) and they claimed that this strong southward transport was due primarily to a strong standing eddy that developed rapidly during the dust input phase of the simulation and rapidly diminished after sol 5. However, in their parallel simulation the same as this baseline simulation but with spatially invariant topography, thermal inertia and albedo fields, this southward dust transport was not so strong as in the baseline simulation. However, at that time, there was not enough observational data to verify their model simulations directly.

In 1989 the grid-based LMD (Laboratoire de Météorologie Dynamique) Martian GCM was developed on the basis of the LMD terrestrial climate model, which was used on earth for weather forecasting or climate change studies [Forget et al., 1999]. A new radiative transfer code and a self-consistent parameterization for the condensation and sublimation of CO₂ were developed to adapt to the Martian atmospheric conditions. Reasonable seasonal and transient pressure variations were able to be reproduced by this model, the first to simulate a full Martian year without any forcing other than insolation. [Hourdin et al., 1995; Collins et al., 1996].

Around this time, a GCM with a physical package similar to the Ames model was developed at the Geophysical Fluid Dynamic Laboratory (GFDL), Princeton, USA. The GFDL Mars GCM was adapted from the GFDL Skyhi GCM [Hamilton, 1995; Wilson and Hamilton, 1996]. The model has since been used to study many different phenomena on Mars, such as Martian thermal tides [Wilson and Hamilton, 1996], surface winds [Fenton and Richardson, 2001] and dust cycle [Basu et al., 2004]. In the study of Basu et al. [2004], they mainly investigated the capability of simulating the

dust cycle and related temperature fields by the GFDL Mars GCM with a similar approach to treating dust lifting as described in the work of Newman et al. [2002a]. Through their model experiments, they obtained a set of parameters to provide a “best fit” model climate based on Dust Devil lifting responsible for the seasonal haze cycle and Wind Stress lifting responsible for dust storms. For a year without a major dust storm, the comparison between observations and temperature fields predicted by their model in terms of “best fit” tuning is shown in Figure 1.10. From Figure 1.10 a and b, it indicates that not only had “global mean” temperatures been produced reasonably, but also the meridional gradients. Specifically, the double-peak feature of air temperatures in the mid-latitudes in both hemispheres, and local minimum in the tropics during summer could be observed in their model results. In Figure 1.10c, the difference between the GCM output and the TES observations suggested that their

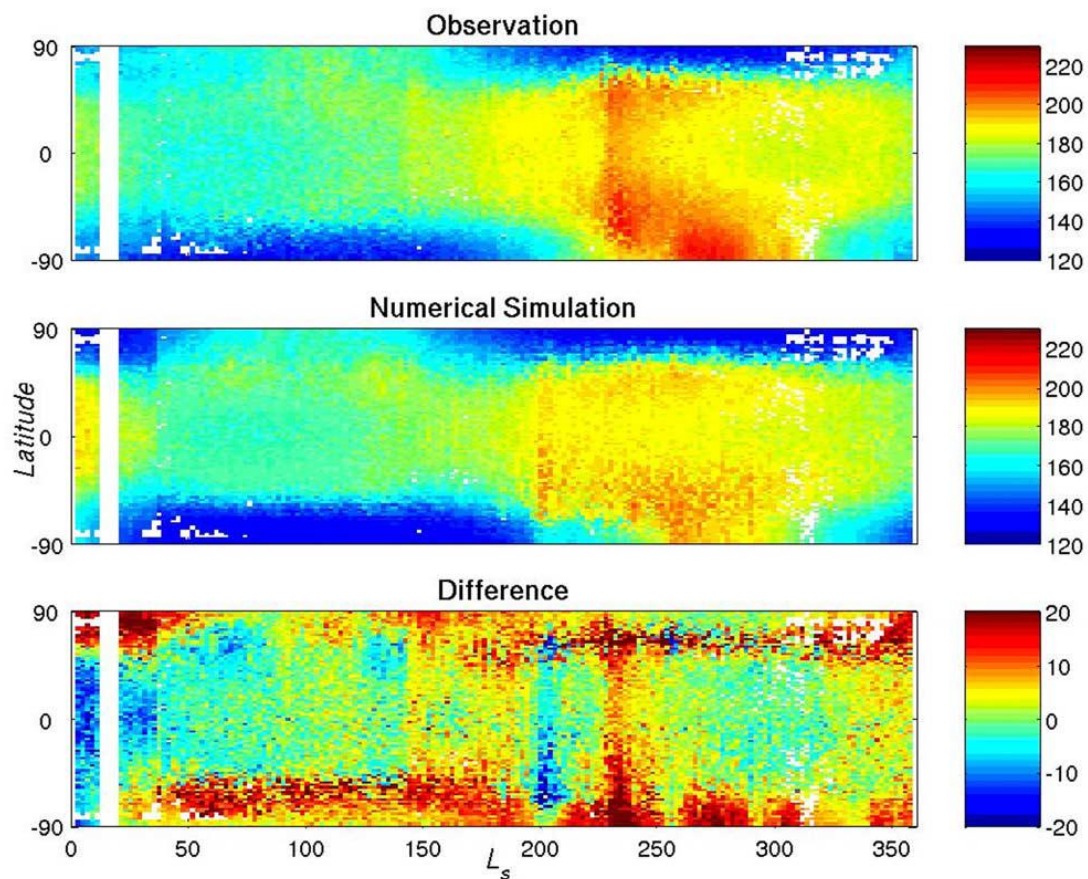


Figure 1.10. A comparison of zonal-mean 15 mm channel temperatures derived from the MGS TES spectra and from the GCM. The GCM output was sampled using the TES observational pattern to maximize comparability. A full annual cycle is shown for each, along with the difference between the model and data. The results are for a nonglobal dust storm year (the first MGS mapping year from northern summer and rolling around into the second) and from the “best fit” GCM simulation. (from the work of Basu et al., 2004)

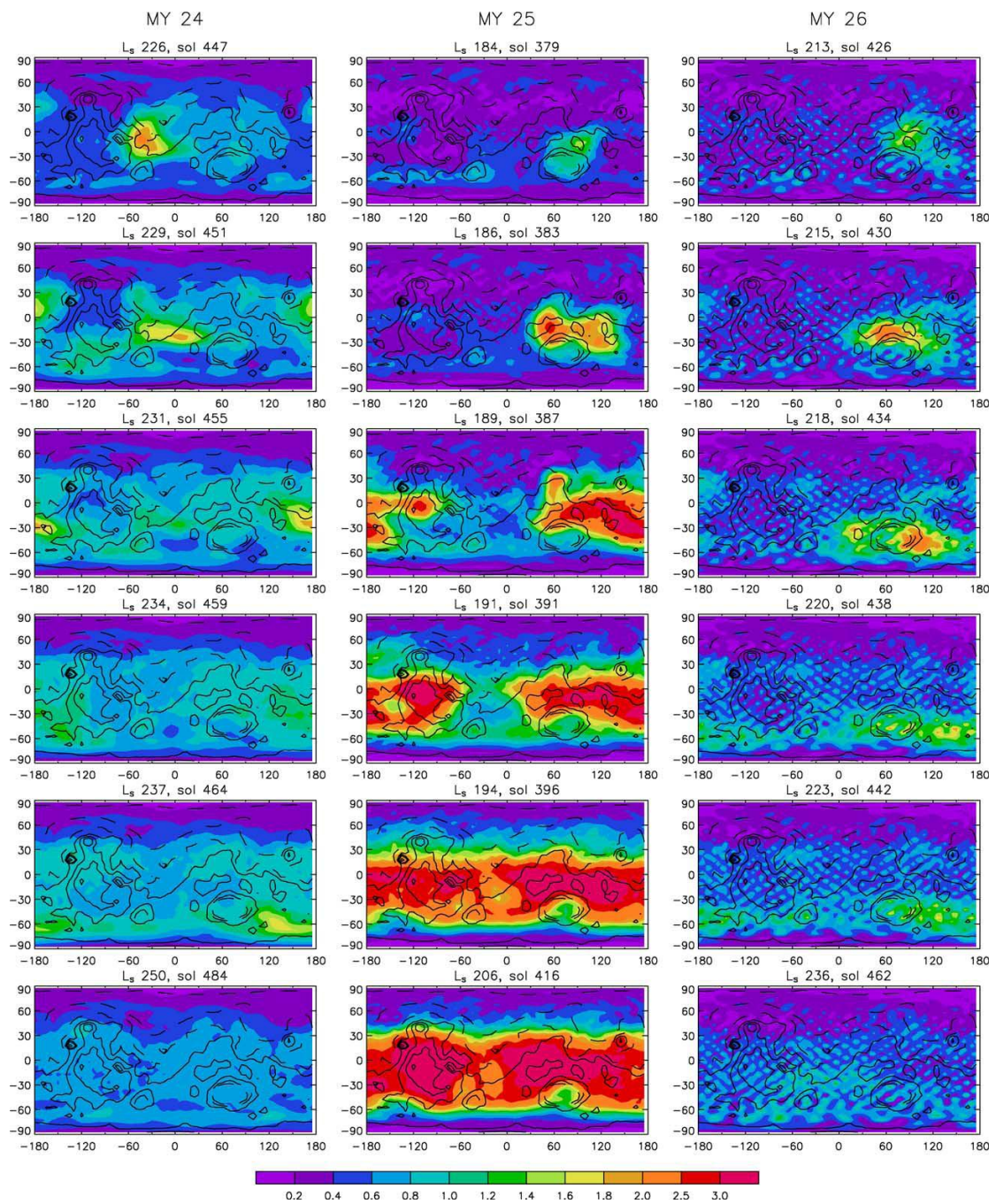


Figure 1.11. Evolution of dust storms in MY 24-26. All the snapshots show the latitude-longitude distribution of the dust total optical depth normalized to 700 Pa. Note the dramatic time scale of the growth of the regional storm between Hellas and Isidis Planitia up to planetary scale in MY 25: it only took 18 sols to encircle the entire planet with an average dust loading three times larger than that in the other two years. (from the work of Montabone et al., [2005])

model predicted the air temperature in the mid-latitudes and tropics quite well except the relatively large discrepancy at roughly $L_s = 200^\circ$ and $L_s = 235^\circ$. However, for the polar region, large discrepancy ($> 20^\circ$) could be seen in both hemispheres, especially for the southern hemisphere.

Almost at the same time, in the 1990s, a three-dimensional Martian GCM (MGCM) was developed jointly with University of Reading and Oxford in the United Kingdom. The spectral solver used in this MGCM was originally adapted from University of Reading [Hoskins and Simmons, 1975]. But in the vertical direction, levels were still defined in terms of the terrain-following σ coordinate system using a standard finite difference approach. Besides simulating the standard atmospheric properties, the UK MGCM also has the capability (shared with the LMD MGCM since the mid 1990s) of treating the CO_2 , water and dust cycles, CO_2 -ice transformation, as well as data assimilation for temperature and dust [Montabone et al., 2005; Lewis et al., 2005; Montabone et al., 2006a; Montabone et al., 2006b; Lewis et al., 2007; Wilson et al., 2008; Rogberg et al. 2010]. In the work of Montabone et al. [2005], data assimilation for temperature profiles and total dust opacity was employed to provide the best-fit model outputs. Not only was the interannual variability of different atmospheric properties described, but also the evolution of dust storm in Martian year (MY) 24-26 (see Figure 1.11), including the 2001 planet-encircling dust storm (occurred in MY25). In their study, they pointed out that the localization of major dust storms varied with season. The 2001 planet-encircling dust storm started as a regional storm but developed to a planetary-scale dust storm only within 18 sols because of the eastward migration and the consequent contribution of dust from the Tharsis region and the plains south of the Tharsis ridge. This probably resulted from the positive feedback of the strength of wind stress lifting because of radiative interactions with the dust cloud, which would enhance the dust lifting in turn. In fact, in MY26, some regional storms built up in the same place as at the start of the MY 25 global storm, but did not develop strongly enough to form a planetary-scale dust storm.

1.4 Motivation and objectives

Dust is now included in almost all current state-of-the-art Martian GCMs in some form. The dust in the Martian model simulations is generally treated in one of several different ways: either

- 1) treating dust as prescribed in seasonal and latitudinal dust distribution scenarios in terms of available observations and then repeated in other years, such as the TES

scenario in the study of Kuroda et al., 2008,

2) assuming the dust opacity is horizontally and temporally uniform at a certain reference level (typically 6.1 mbar), and then distributing the dust according to the prescribed vertical profile originally described by Conrah [1975] [Kahre and Haberle, 2010],

3) before transporting the dust in terms of the wind fields and temperature predicted by Martian GCM itself, giving an initial prescribed injection of dust [Murphy et al., 1995],

4) simulating dust transport using the wind fields and temperature predicted by the Martian GCM itself, but with runtime dust sources, i.e. near-surface wind stress lifting and dust devil lifting [Newman et al., 2002a; Basu et al., 2004] or,

5) data assimilation for observed column dust opacity without dust transport, and distributing the dust vertically by scaling of a prescribed (Conrath) profile [Montabone et al., 2005; Lewis et al., 2007].

The methods mentioned above have their own advantages and disadvantages. Method 1) only has reliable information for the column dust opacity according to the limitation of TES observations. Even if vertical information is available in the observed datasets, such as, in MCS limb data, it will still lose the detailed information in space, as well as any annual variability. Method 2) is based on the various idealised assumptions like horizontally and temporally uniform dust opacity and empirically determined vertical dust distributions [Kahre and Haberle, 2010], so it is almost impossible to represent real instantaneous atmospheric conditions. In the method 3) a totally artificial dust source is added at the start of the simulation so that it lacks of the representation of dust lifting mechanisms on Mars and can not therefore make the results physically and numerically reasonable after a relatively long-term simulation. In this case the dust would either spread across most of the planet (as shown in the results of Murphy et al. [1995]) which may not be realistic or possibly settle out by sedimentation. Method 4) has reasonable physical mechanisms to represent the unique dust behaviours on Mars and can therefore produce results in acceptable agreement with real observations. However, no simulation has yet produced the observed amount of interannual variability [Newman et al., 2002b]. Finally, method 5) was able to provide a complete and balanced “best-fit” to the observations, but the dust transport has not been enabled so far because of a lack of vertical information on dust opacity from TES. Thus, the dust would be distributed by scaling the Conrath profile in the vertical and remains static when no observation is available to correct the dust fields.

As discussed above, method 4) should be the most reasonable way of doing dust

simulation on Mars in terms of its physical representation. However, in the light of data and model [Newman et al., 2002a; Newman et al., 2002b] limitations, it is difficult to understand the dust behaviour precisely, which results in a failure to produce some significant features of dust storms, (e.g. the development of 2001 planet-encircling dust storm), as well as the interannual variability of dust. Method 5, on the other hand, in practice generates results that are a “best-fit” to real observations through the data assimilation technique, because of data limitation, absence of a dust transport scheme leads to an unrealistic vertical distribution of dust. This impedes the progress of the research related to the dust, and the capability of providing a realistic reconstruction of the dust storm structures, especially for the 2001 planet-encircling dust storm.

Therefore, it is extremely important to improve the capability of the data assimilation technique on Mars. As MCS datasets become available which contain vertical information on dust opacity, it should be entirely possible to incorporate the dust transport scheme into the data assimilation technique in order to provide a three-dimensional structure of dust storms, corrected by the real observational data.

In this project, the UK Martian GCM will be used as a primary tool to develop more advanced data assimilation scheme for temperature and dust. The aim of this project is to incorporate the data assimilation scheme and the dust transport scheme into the model integration together in a new version of the MGCM. For the data assimilation scheme itself, we will extend the assimilation of column dust opacity to include the capability of assimilating dust profiles, similar to that done for temperature profile in the current model setting.

With this new development of MGCM data assimilation, UK MGCM will be a powerful tool to investigate dust activity on Mars. Corrected opacities will be appropriately converted to dust mixing ratios, and further used to reconstruct the dust transport and diagnose the degree to which it is predicted in the model. It will be able to provide three-dimensional information on the dust distribution for the further study of the evolution of dust storms, as well as the atmospheric properties affected by dust storms. What is more, it will provide insight to investigate the interannual and interseasonal variability of Martian climate. It also offers possibility of improving the dust lifting schemes themselves. Given that the temperatures and winds are basically correct in the reanalysis, the correction of the dust field becomes solely a test of the accuracy of lifting parameterizations, as well as the assumptions about surface dust availability. To some more extent, this study can perhaps also provide information

towards planning the future Exomars Climate Sounder (EMCS) investigation [Schofield et al., 2011], as well as other possible applications of the observational data.

Chapter 2 Martian General Circulation Model

A three-dimensional Martian General Circulation Model (MGCM) has been used to study the Martian Atmosphere [Forget et al., 1999]. Further, based on this MGCM, data assimilation has been applied in several studies [Montabone et al., 2005; Lewis et al., 2005; Montabone et al., 2006a; Montabone et al., 2006b; Lewis et al., 2007; Wilson et al., 2008; Rogberg et al. 2010] as an effective tool with which to analyze spacecraft observations and phenomena (e.g., atmospheric tides, transient wave behavior, effects of clouds in the tropics, weather predictability, etc.) in the Martian atmosphere. The MGCM employed in my study combines a spectral dynamical solver and a tracer transport scheme developed in UK and Laboratoire de Météorologie Dynamique (LMD; Paris, France) physics package developed in collaboration with Oxford, The Open University and Instituto de Astrofísica de Andalucía (Granada, Spain).

In this chapter, the details of MGCM will be described, for instance, model dynamics, physics parameterizations and so forth. Besides, the description of data assimilation scheme, which has been implemented in the MGCM, is included as well.

2.1 Model Dynamics

The dynamical core of our MGCM is based on a spectral solver which was adapted from University of Reading [Hoskings and Simmons, 1975]. With further extension, the total wavenumber for triangular truncation is 31 corresponding to 72×36 real space grids in longitude \times latitude.

In the vertical direction, levels are defined in terms of the terrain-following σ coordinate system using a standard finite difference approach. The first three of 25 vertical levels close to surface are at heights of 4, 19 and 44 m above surface, and this enhanced vertical resolution near the surface provides the capability of resolving detailed surface processes represented in the model. The middle of the top layer is at an altitude of 80 km. Some advantages coming with this extension are that it enables us to explore the meteorological phenomenon at higher altitudes and such a deeper model domain allows the unconstrained development of the Hadley circulation and is important to obtain a better simulation [Forget et al., 1999]. At the three uppermost levels, sponge layers are used with the purpose of reducing the spurious reflections of vertically propagating waves from the model top. A linear drag is added to the eddy

components of the vorticity and divergence fields.

The basic equations for a hydrostatic, adiabatic and inviscid gas surrounding a rotating spherical planet are cast in vorticity-divergence form as [Hoskings and Simmons, 1975],

Vorticity equation

$$\frac{\partial \zeta}{\partial t} = \frac{1}{1 - \mu^2} \frac{\partial F_V}{\partial \lambda} - \frac{\partial F_U}{\partial \mu}$$

Divergence equation

$$\frac{\partial D}{\partial t} = \frac{1}{1 - \mu^2} \frac{\partial F_U}{\partial \lambda} + \frac{\partial F_V}{\partial \mu} - \nabla^2 \left(\frac{U^2 + V^2}{2(1 - \mu^2)} + \phi + \bar{T} \ln p_* \right)$$

First law of thermodynamics

$$\frac{\partial T'}{\partial t} = -\frac{1}{1 - \mu^2} \frac{\partial (UT')}{\partial \lambda} - \frac{\partial (VT')}{\partial \mu} + DT' - \dot{\sigma} \frac{\partial T}{\partial \sigma} + \kappa \frac{T\omega}{p}$$

Continuity equation

$$\frac{\partial \ln p_*}{\partial t} = -V \cdot \nabla \ln p_* - D - \frac{\partial \dot{\sigma}}{\partial \sigma}$$

Hydrostatic balance

$$\frac{\partial \phi}{\partial \ln \sigma} = -T$$

Here

$$F_U = V\zeta - \dot{\sigma} \frac{\partial U}{\partial \sigma} - T' \frac{\partial \ln p_*}{\partial \lambda},$$

$$F_V = -U\zeta - \dot{\sigma} \frac{\partial V}{\partial \sigma} - T'(1 - \mu^2) \frac{\partial \ln p_*}{\partial \mu}.$$

The notations of the variables are as follows,

ζ : absolute vorticity

D : divergence
 $T = \bar{T}(\sigma) + T'$: temperature
 p_* : surface pressure
 p : pressure
 ϕ : geopotential
 $\sigma = p / p_*$: sigma vertical coordinate
 λ : longitude
 θ : latitude
 μ : $\sin \theta$
 u : zonal velocity
 v : meridional velocity
 U : $u \cos \theta$
 V : $v \cos \theta$
 R : specific gas constant
 c_p : specific heat capacity of dry air at constant pressure
 κ : R / c_p

2.2 Surface Processes

The balance between incoming fluxes and thermal conduction in the soil contributes to changes of surface temperature. Together with the surface thermal inertial field derived from TES data and Viking observations [Forget et al., 1999], the accurate measurement of detailed topography of Mars from the Mars Orbiter Laser Altimeter (MOLA) aboard Mars Global Surveyor is used to calculate the surface processes.

2.3 Subgrid Dynamics

The turbulent mixing in the vertical of any state variable a is computed as

$$\frac{\partial a}{\partial t} = \frac{1}{\rho} \frac{\partial}{\partial z} K \rho \frac{\partial a}{\partial z}$$

where K takes different values K_u for (u, v) and K_θ for θ . The turbulent surface flux in the bottom layer is represented by $\rho C_d U_1 (a_1 - a_0)$, where a_1 and a_0 are the variable values in the first model layer and at the surface, U_1 is the wind velocity in the first layer, and C_d is the drag coefficient. In the model, we simply use

$$C_d = \left(\frac{\kappa}{\ln \frac{z}{z_0}} \right)^2$$

here, κ represents the von Karman constant, which is assumed to take the value 0.4 and z_0 is the roughness coefficient which is chosen to be 0.01 m everywhere on Mars suggested by Sutton et al. [1978] for the Viking Lander sites.

Based on an equation for evolution of the turbulent kinetic energy (TKE) [Mellor and Yamada, 1982], the mixing coefficients are computed. The evolution of TKE can be obtained from

$$\frac{\partial E}{\partial t} = \frac{q^3}{l} \left(S_u G_u + S_\theta G_\theta - \frac{1}{b_1} \right) + \frac{\partial}{\partial z} K_E \frac{\partial E}{\partial z}$$

where,

$$q = \sqrt{2E}$$

$$M = \sqrt{\left(\frac{\partial u}{\partial z} \right)^2 + \left(\frac{\partial v}{\partial z} \right)^2}$$

$$G_u = \frac{l^2}{q^2} M^2$$

$$G_\theta = -\frac{l^2}{q^2} \frac{g}{\theta_0} \frac{\partial \theta}{\partial z}$$

$$S_u = \frac{\alpha_1 + \alpha_2 G_\theta}{(1 + \alpha_3 G_\theta)(1 + \alpha_4 G_\theta)}$$

$$S_\theta = \frac{\alpha_5}{1 + \alpha_3 G_\theta}$$

$$S_E = \alpha_6$$

The coefficients $\alpha_1, \alpha_2, \alpha_3, \alpha_4, \alpha_5, \alpha_6, b_1$ are assigned the constant values 0.393, -3.09, -34.7, -6.13, 0.494, 0.38, 16.6 [Forget et al., 1999].

2.4 Dust lifting mechanisms

2.4.1 Dust lifting by near-surface wind stress

The vertical flux of lifted dust V_N is assumed to be proportional to the horizontal saltation flux of sand [Montabone et al., 2005]:

$$V_N \propto \frac{1}{\sqrt{\rho}} \left(\zeta^{\frac{3}{2}} + \zeta \zeta_t^{\frac{1}{2}} - \zeta^{\frac{1}{2}} \zeta_t - \zeta^{\frac{3}{2}} \right)$$

where ρ represents the near-surface air density, ζ represents the near-surface wind stress magnitude and ζ_t represents an empirically determined stress threshold for the lifting to occur. The near-surface wind stress ζ is related to the near-surface wind speed U by,

$$\zeta = \rho \left(\frac{\kappa U(z)}{\ln(z/z_0)} \right)^2$$

where κ represents von Karman's constant, z is the average height of the lowest layer above the surface and z_0 is the height at which velocities are zero (i.e. roughness height, taken as 0.01m everywhere on Mars).

2.4.2 Dust lifting by the activity of dust devils

The flux of dust lifted by the activity of dust devils η (i.e. the thermodynamic efficiency of the dust devil convective heat engine) is obtained by

$$\eta \equiv 1 - \frac{p_s^{\chi+1} - p_{top}^{\chi+1}}{(p_s - p_{top})(\chi + 1)p_s^\chi},$$

where p_s represents the surface pressure, p_{top} represents the pressure at the top of the convective boundary layer (defined in the model where TKE drops down to a threshold of $0.5 \text{ m}^2 \text{ s}^{-2}$), and χ represents the specific gas constant divided by the specific heat capacity at constant pressure. The energy to drive any dust devil is determined by the temperature difference of surface to air, while the thermodynamic efficiency relate to how high the dust devils are able to grow [Rennó et al., 1998].

2.5 Data assimilation

A data assimilation scheme combined with a Martian Global Circulation Model (MGCM) is able to provide a complete, balanced, four-dimensional solution consistent with observations. This technique has been applied in several previous studies to give us a better understanding of phenomena in the Martian atmosphere given incomplete and/or noisy measurements [Montabone et al., 2005; Lewis et al.,

2005; Montabone et al., 2006a; Montabone et al., 2006b; Lewis et al., 2007; Wilson et al., 2008; Rogberg et al. 2010]

The data assimilation scheme implemented in the MGCM is computationally inexpensive compared to MGCM itself, and based on the analysis correction sequential estimation scheme [Lorenc et al., 1991], but with modifications specific to Mars [Lewis et al., 2007].

The analysis iteration, which is based on the least-squares sense, is performed at each dynamical time step of the model (currently 480 times per sol at the chosen resolution), and attempts to make the model predictions fit to the observations in terms of their relative errors. Observational increments to the model are determined in time and space in terms of empirical covariance functions.

For the current study, only temperature profiles and measurements of total dust opacity have so far been assimilated into the MGCM at each horizontal grid point. After the analysis correction of the temperature field, the temperature increments are balanced by non-divergent, thermal wind increments. Thus, the wind fields will be adjusted slightly consistent with the geostrophic thermal wind balance.

The analysis correction of temperature profiles was performed in the vertical direction followed by the horizontal and temporal analysis. The temperatures are interpreted as mean temperatures between a standard set of pressure values, which can represent the resolution of the vertical temperature retrievals. The corresponding model layer thickness is calculated between each pressure value in terms consistent with the temperature retrievals. The philosophy behind this method is that the vertical scale of temperature increments should reflect the observational resolution instead of the model vertical resolution. This method also has the advantage of maintaining detailed features in the vertical direction which are predicted by the dynamics and physics of the model itself, even if this can not be resolved explicitly by the remotely-sensed data.

In the horizontal space, the increments to the model variables on each model grid, Δx_k are spread by the following function [Lorenc et al., 1991],

$$\Delta x_k = \lambda \sum_i \mu_{ki} \bar{Q}_i R_i^2 (\delta t_i) C_i$$

where,

k : refers to a model grid point

i : refers to an observation

\bar{Q}_i : is a function of the ratio of observational to first guess error and of the local observation density around each observation location.

R_i^2 : is a function used to determine how the observational increments are spread in time

δt : is the time difference between model time and observation time (see Figure 2.1).

C_i : is the increments at the observation locations.

λ and μ_{ki} will be explained in detail afterwards.

In practice, the model will read in the observation data 5h before they are valid and finally discards them 1 h after their valid time.

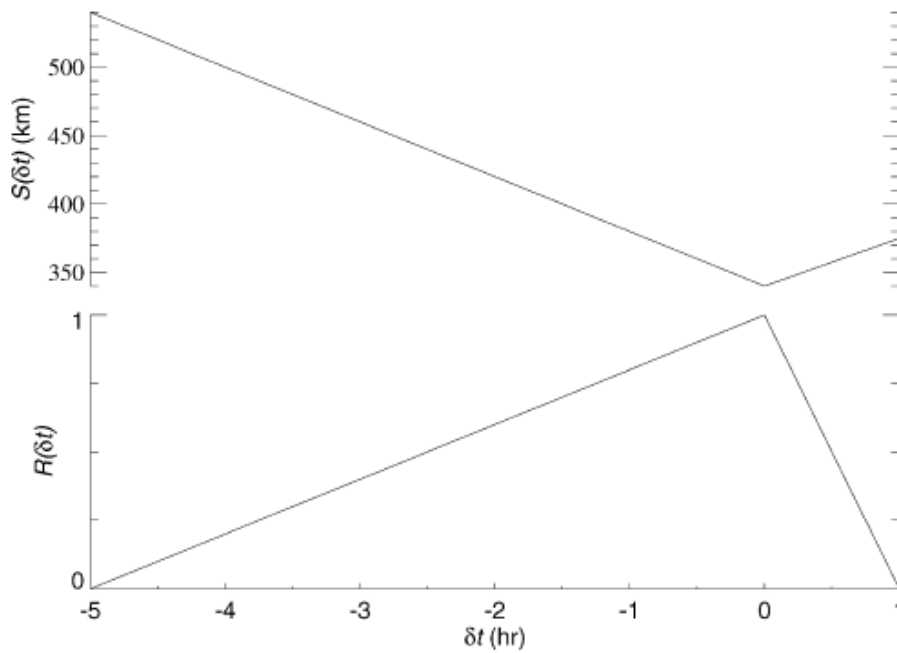


Figure 2.1, Horizontal correlation scale, S , and time factor, R , as a function of the model-observation time difference, δt . (from the work of Lewis et al., 2007)

The observational increments are spread by a second-order auto regressive function of the distance, r_{ki} , between the location of observation i and each model grid point k ,

$$\mu_{ki} = (1 + r_{ki} / S_i(\delta t_i)) \exp(-r_{ki} / S_i(\delta t_i))$$

where $S(\delta t)$ is the correlation scale of the function, taken to be large at $\delta t = -5h$,

and a minimum at $\delta t = 0h$. Overall, the increment will reduce by a factor of half over nearly 570 km distance, but the maximum radius of influence is chosen at 1200 km.

The parameter λ is related to the nudging relation with nudging coefficient G by

$$G = \lambda / (1 - \lambda) \Delta t$$

Here, Δt is the model dynamical time step. G was set to $5 \times 10^{-4} s^{-1}$ with a linear reduction, between 30 and 20 latitude in both hemispheres to $4 \times 10^{-4} s^{-1}$ at equator.

However, in the current model setup, data assimilation of total dust opacity is only conducted without advecting the dust mainly because it is to simplify the first attempt to take dust variations into account. Therefore, the vertical distribution of the dust opacity τ at the given latitude, longitude and time is determined by an empirical relation of the form,

$$\tau = \tau_{ref} \cdot \exp\left\{a \left[1 - (p_0/p)^{(b/z_{max})}\right]\right\}$$

For pressure $p \leq p_0$, where p_0 is taken to be $p_0 = 700 Pa$, and with $\tau_{ref} = \tau$, for $p > p_0$, τ_{ref} is the total dust opacity at reference level (700 Pa), latitude, longitude and time. a and b are constant with values $a = 0.007$, $b = 70 km$. z_{max} is the ‘top’ of the dust layer, varying with solar longitude L_s and latitude ϕ determined by

$$z_{max} = 60 + 18 \sin(L_s - 160^\circ) - \sin^4 \phi [32 + 18 \sin(L_s - 160^\circ) - 8 \sin(L_s - 160^\circ) \sin \phi]$$

In the new work described in this report, the assimilation of dust measurements has been extended to allow for the advection of dust by the winds simulated by the model. The details of recent development for combining the dust transport and the assimilation of total dust opacity will be addressed in the chapter 4 (2-D Data Assimilation of Column Dust Opacity with Dust Transport).

Chapter 3 Interannual and Interseasonal Variability of

Martian Climate using Data Assimilation: A Semi-Annual

Oscillation

In the upper stratosphere and mesosphere of Earth, the semi-annual oscillation (SAO) of the mean zonal wind in the tropical stratosphere and mesosphere is found as a clear feature [Reed, 1966; Garcia et al., 1997]. Reed [1966] used observational data to study the semi-annual cycle of zonal wind on Earth. He pointed out that the strongest westerly winds occur shortly after the equinoxes in the lower mesosphere and later extended to the lower levels. The pronounced semi-annual oscillation happens at intermediate and upper levels, and the amplitude of the semi-annual component reaches a peak at about the height of the stratopause. Similar features in the Martian tropics (between 10°S and 10°N) have been studied in the work of Kuroda et al. [2008]. Here, we are going to present some actual observations of the SAO phenomenon on Mars derived from assimilated model (MGCM) results, but in contrast to the study of Kuroda et al., extended to the atmosphere of the whole planet. We divide the atmosphere into 7 latitude bands (60°N and 90°N, 40°N and 60°N, 10°N and 40°N, 10°S and 10°N, 10°S and 40°S, 40°S and 60°S, 60°S and 90°S). In each latitude band, not only will the actual zonal-mean of daily-averaged zonal wind be presented and discussed in this chapter, but also the results of a singular Spectrum Analysis (SSA) of daily averaged zonal-mean zonal wind, including the amplitudes of the first 6 Principal Components (PCs) evolving with time, corresponding eigenvector height-time contour maps which isolate and capture the semi-annual oscillation component and reconstructions of the magnitude of semi-annual oscillation components will be analyzed.

3.1 Previous work on semi-annual oscillations on Mars

In the work of Kuroda et al. [2008], a clear SAO phenomenon between 10°S and 10°N, similar to the stratospheric SAO in the Earth in terms of appearance, is described in their results from a free-running Martian General Circulation Model (GCM; see Figure 3.1 for their results of semi-annual oscillation). Their simulations were run for 7 model Martian years initialized from an initial isothermal and windless state, and the last 5 years output were used to conduct their study on Martian semi-annual oscillations.

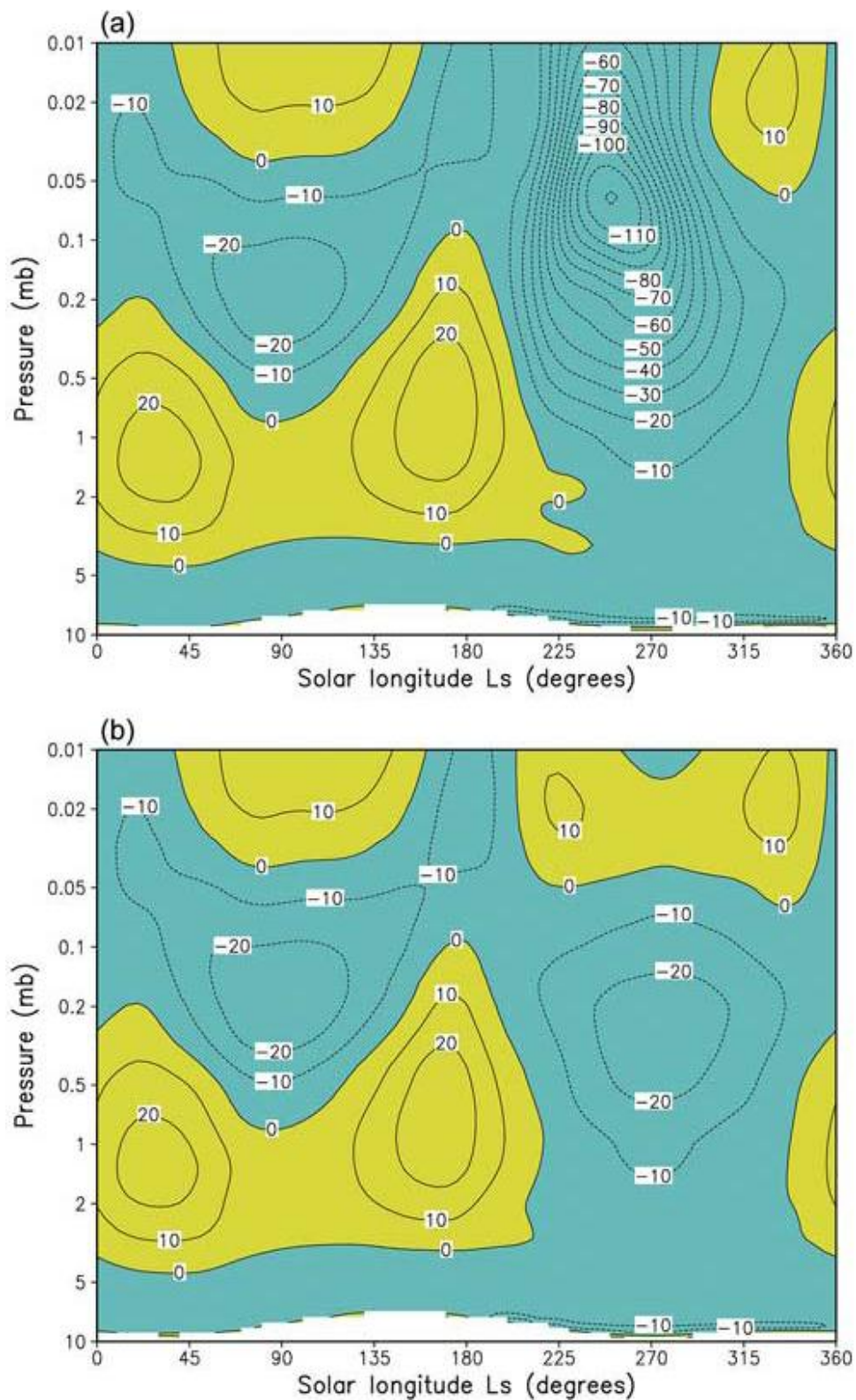


Figure 3.1. (a) The composite annual cycle of the simulated mean zonal wind averaged between 10°S and 10°N from the run with TES2 dust scenario. The contour interval is 10 m s⁻¹, westerly wind is shaded with yellow, (b) Same as a, except from the run with the seasonally uniform dust opacity ~0.2. (from the work of Kuroda et al. [2008]).

Two scenarios were conducted by Kuroda et al. [2008] to demonstrate the semi-annual oscillation on Mars. One was run with a prescribed dust opacity representing the MGS-TES retrievals (shown in Figure 3.1a), and the other was run with a seasonally uniform dust opacity (~ 0.2 ; Figure 3.1b). Afterwards, the simulated zonal wind was averaged between 10°S and 10°N temporally and horizontally to obtain the mean annual cycle.

In Figure 3.1a, it is seen that a clear semi-annual oscillation feature can be observed in the middle atmosphere especially between 0.2 and 1mb. In the first quarter of the year, the mean zonal wind changes from westerly to easterly between 0.2-1mb, or the westerly component increases in some altitudes. During the second quarter of the year, the mean zonal wind changes back to easterly in the corresponding altitudes, or the westerly component decreases. Thus, a full cycle of a semi-annual oscillation completes, and a new cycle will start. However, on comparing the two cycles within one year, it seems that the oscillation in the second half year is stronger in terms of the zonal wind gradient and penetration in the vertical direction. In the other scenario (Figure 3.1b), in which the simulation is repeated with seasonally uniform dust opacity, a similar semi-annual oscillation can be seen but with relatively equal magnitude in the second half year compared to the scenario with MGS-TES dust variations.

3.2 Study of semi-annual oscillation with our MGCM

In this section, we present actual observations (nearly 3 Martian years in total) of SAO phenomena on Mars derived from assimilated model results in different latitude bands (60°N and 90°N , 40°N and 60°N , 10°N and 40°N , 10°S and 10°N , 10°S and 40°S , 40°S and 60°S , 60°S and 90°S) which are based on a reanalysis using the UK MGCM with a data assimilation scheme which assimilates Mars Global Surveyor/Thermal Emission Spectrometer (MGS/TES) retrievals of temperature and column dust opacity. The detailed model setup was described in Chapter 2, and the data assimilation scheme employed in this study was introduced in the work of Lewis et al.[2007]. The pressure and pseudo-altitude values in the following figures are simply calculated from the model terrain-following vertical sigma coordinate using a reference pressure of 6.1mb and a scale height of 10.8km.

In the same latitude band (10°S and 10°N) that was chosen to discuss the semi-annual oscillation in the work of Kuroda et al. ([2008]; Figure 3.1), a similar semi-annual oscillation phenomenon can be observed in our 3-year results (left panel

Figure 3.2), but extending to higher altitude. Between 0.01mb and 0.75mb, there is a significant zonal-mean wind speed increase from $L_s = 240^\circ$ to $L_s = 345^\circ$ in each year, and one of the two cycles in each year looks stronger than the other. It is noticeable that when the 2001 planet-encircling dust storm occurred (MY 25), this event had a significant impact also on the equatorial zonal wind, as can be clearly seen in Figure 3.2, which show that low-altitude westerly (usually around 15 km altitude) was strongly reinforced and extended in altitude.

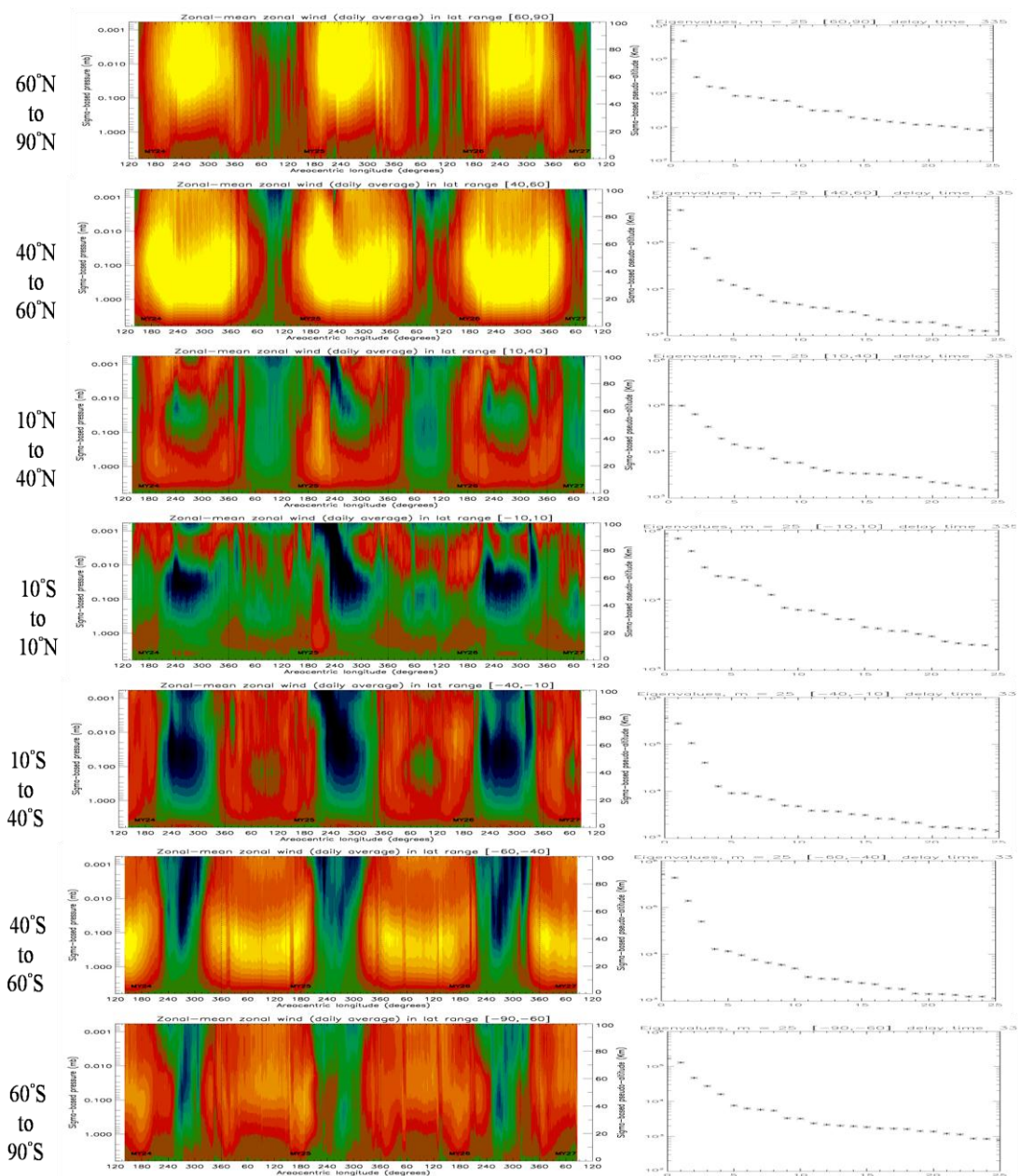


Figure 3.2. the raw zonal-mean of daily-averaged zonal wind in different latitude bands (left) and the first 26 eigenvalues for the zonal-mean zonal wind of SSA analysis in different latitude bands (right).

Not only do we show the reanalysis results on the equator here, but we also examine the results extending over to the whole planet in the series of latitude bands defined above (left panel in Figure 3.2). From these, it is clear that the semi-annual oscillation actually extends across the whole planet. The pattern is quite noticeable in the middle atmosphere of the latitude band 10°N and 40°N, for example, and the signature of the 2001 planet-encircling dust storm can be seen clearly in this latitude band. Within each latitude band, one of two semi-annual cycles appears to be more noticeable extending from the very low atmosphere to near the top of the model. It is probably because the annual cycle strengthens the signal of semi-annual oscillation when these two signals overlap each other in the same phase, however, no clear conclusion can be drawn without further examination of SAO mechanism. It is interesting to point out that within the annual cycle, the periods with easterly winds in all altitudes exhibit a phase-shift between the northern and southern hemispheres, which may have a strong correlation with the summer season in each hemisphere.

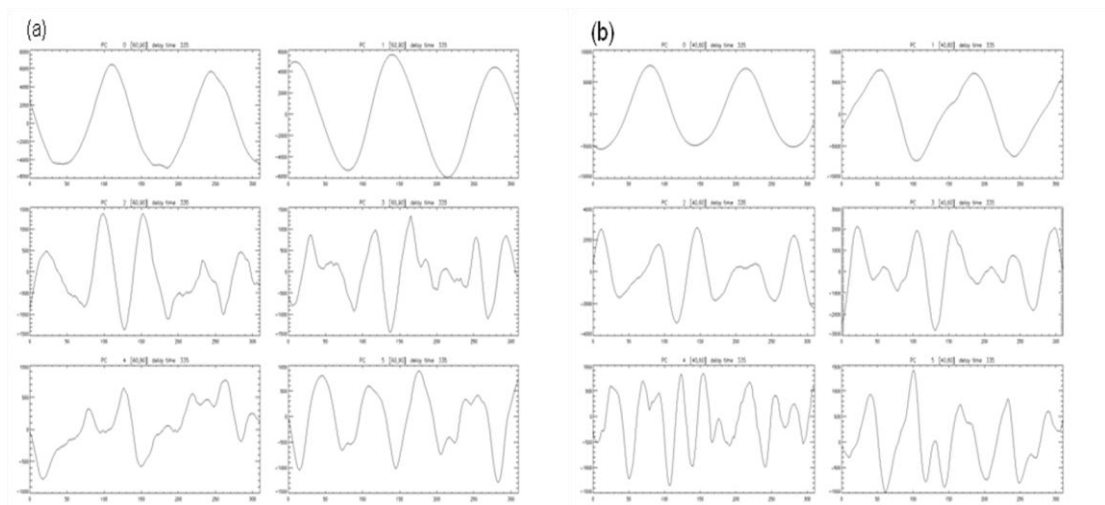
We perform a Singular Spectrum Analysis (SSA) of daily averaged zonal-mean zonal wind, which is used to adaptively isolate the semi-annual variations in each latitude band. SSA is a statistical technique applied in the time domain, and similar to the EOF analysis which is applied in the spatial domain. It is widely used in signal processing [Pike et al., 1984]. Compared to other types of spectral analysis, the filters used in SSA are not prescribed a priori, but are determined, optimally, from the data themselves. SSA is well suited to detect and analyze weak oscillations in a noisy system [Ghil et al., 1990].

In order to smooth the day-to-day fluctuations of zonal wind fields, a 5-day running-mean is applied to the diurnally sampled zonal-mean zonal wind. Afterwards, the data was resampled by choosing every 5 data points for SSA analysis. The analysis time window here was chosen to be 335 days (67 data points being resampled by choosing every 5 data points) which is approximately half a Martian year. It has been tested that the results were not sensitive to the choice for this time window in terms of period of semi-annual oscillation over a reasonable range. The first 26 eigenvalues for the SSA analysis of zonal-mean zonal wind in different latitude bands are shown in Figure 3.2 as well (right panel) to give an impression of the relative importance of each eigenvalue.

Because the first 6 eigenvalues in total already capture a large contribution to the variance of the final solution of zonal wind, their frequencies (and other

characteristics) will be discussed in detail (shown in Figure 3.3). In the middle (40°N and 60°N Figure 3.3(b), 40°S and 60°S Figure 3.3(f)) and high (60°N and 90°N Figure 3.3(a), 60°S and 90°S Figure 3.3(g)) latitude bands, the first two PCs normally present an annual oscillation, while in the low latitude bands (10°N and 40°N, 10°S and 40°S) and equator (10°S and 10°N), the main features of the annual oscillation still dominates but with the influence of a semi-annual oscillation perturbation. It means the annual oscillation component still contributes most to the zonal-mean zonal wind variations at these latitudes, but in the middle and high latitude bands it seems its impact is more prominent, whereas, in the lower latitudes and equator, the semi-annual oscillation feature can be seen in the first two PCs as well.

In all the latitude bands, the third and fourth PCs represent the semi-annual oscillation (Figure 3.3). In each latitude band, five relatively clear cycles can be seen during the whole analysis period. However, in the southern atmosphere including 10°S and 40°S, 40°S and 60°S, 60°S and 90°S, this feature is more obvious in both the third and fourth PCs, and the amplitudes are almost equal. In the northern hemisphere, one of the two PCs in each latitude band is relatively clear, while the other one has some small features on top of the semi-annual cycles which could be impacts of higher frequency waves. On the equator, the fourth PC shows some features with similar amplitude structure to the semi-annual signal. It suggests that semi-annual signal can not be so significant on the equator as in other latitude bands, but the reason of this phenomenon still needs further investigation for the SAO mechanism.



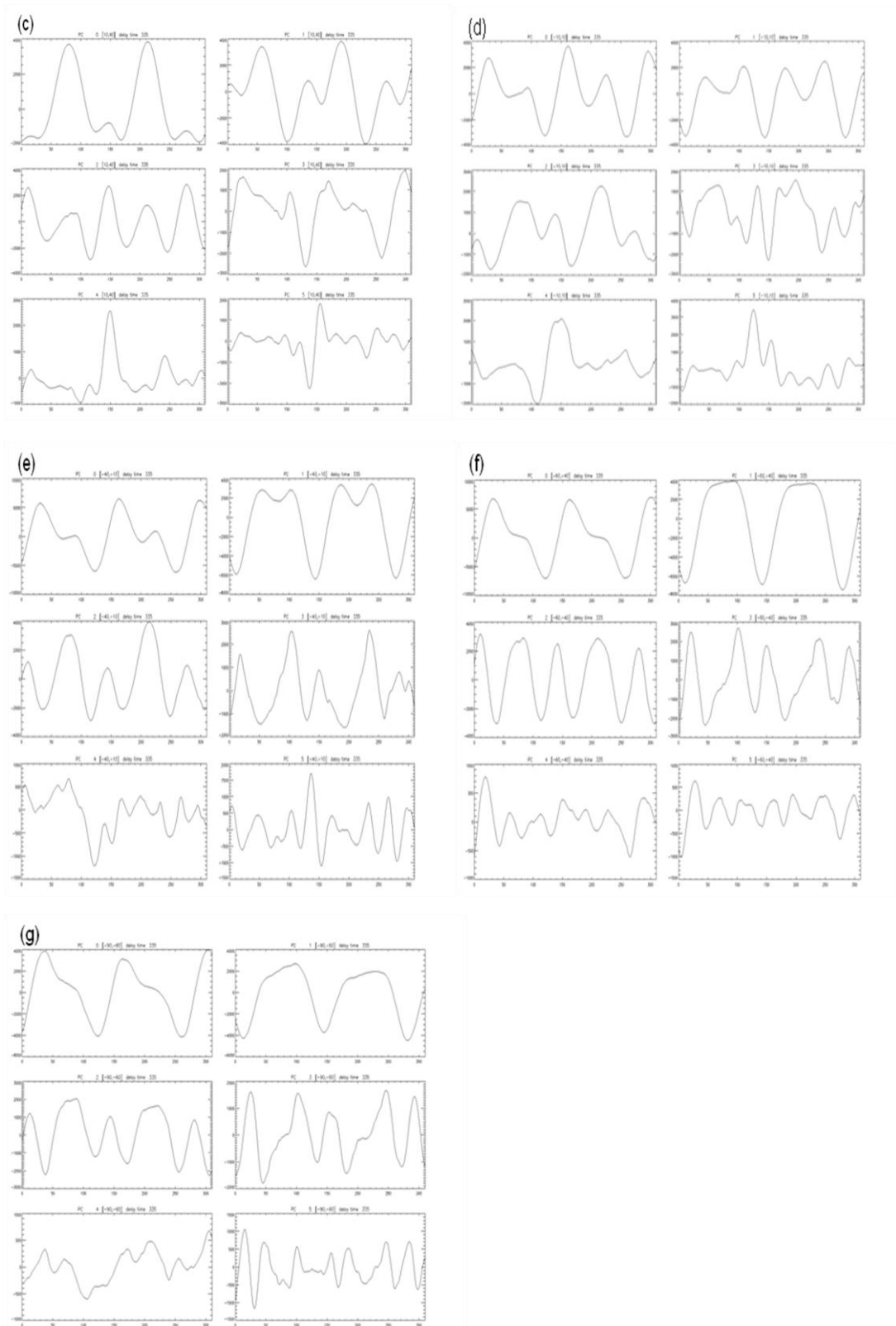


Figure 3.3. The PCs of the first 6 eigenvalues in different latitude bands. In each figure the upper two is the first pair of PCs, the middle two is the second pair and the lower two is the third pair of PCs, (a) for 60°N and 90°N, (b) for 40°N and 60°N, (c) for 10°N and 40°N, (d) for 10°S and 10°N, (e) for 10°S and 40°S, (f) for 40°S and 60°S, (g) for 60°S and 90°S.

The fifth and sixth PCs in high latitudes of the northern hemisphere (60°N and 90°N) also indicate some semi-annual oscillation signal. However, in most of the other latitude bands, the fifth and sixth PCs appear to represent the high-frequency patterns, especially in the southern hemisphere. Besides, it is interesting to mention that these two PCs in the low latitudes of the northern hemisphere (10°N and 40°N) and equator (10°S and 10°N) shows some abrupt changes of amplitude during the 2001 planet-encircling dust storm (MY 25). The further relationship among these two components, corresponding to an increase of actual zonal wind and perhaps contributing further to trigger the 2001 planet-encircling dust storm could be an interesting topic to investigate further in future.

Within the chosen analysis time window (335 days) for SSA analysis, height-time plots present the distribution of semi-annual oscillation activity in terms of height and time (Figure 3.4). It is obvious that in each latitude band a slight phase difference can be seen between the third eigenvector and fourth eigenvector, i.e. the signals represented by the third eigenvector almost start from the highest positive value then change to the lowest negative value, and back to the positive value again, while the signals represented by the fourth eigenvector except at the equator start from a positive value but change quickly to low values, and go through a full half-cycle to negative values again. It indicates that the phase of the fourth eigenvector can be near 45° ahead of the phase of the third eigenvector, and probably the oscillation cycle of fourth eigenvector is slightly shorter than for the third eigenvector. It is noticeable that the clear semi-annual oscillation signals can penetrate all the way to the upper atmosphere from the lower atmosphere in each latitude band, and the maximum in amplitude of the semi-annual oscillation happens in the middle atmosphere. However, this phenomenon is more significant in the middle and high latitude bands of the northern hemisphere (60°N and 90°N, 40°N and 60°N) and the southern hemisphere (10°S and 40°S, 40°S and 60°S, 60°S and 90°S)

The third and fourth PCs in the SSA analysis are also reconstructed to demonstrate the semi-annual oscillation components in terms of daily-averaged zonal-mean zonal wind in different latitude bands (see Figure 3.5). Between 10°S and 10°N, the pattern represented by these two PCs in reconstruction is relatively complicated, perhaps because dynamical conditions at the equator can be strongly affected by plenty of factors. But the semi-annual oscillation can be observed extremely clearly in the middle atmosphere (altitude 40km ~ 80km) even in the raw zonal-mean of daily-averaged zonal wind at the equator (10°S and 10°N) and the low latitude bands

regardless of hemisphere (10°N and 40°N , 10°S and 40°S). Extending to the polar regions, the semi-annual oscillation becomes more significant, but the overall amplitude reaches its maximum in the middle latitude bands (40°N and 60°N , 40°S and 60°S) in both hemispheres. However, unlike at the equator and at low latitudes, one of two semi-annual oscillations in the middle latitude bands (40°N and 60°N , 40°S and 60°S) and the high latitude bands (60°N and 90°N , 60°S and 90°S) are not found in the corresponding raw zonal-mean of daily-averaged zonal wind. Furthermore, it is noticeable that within each latitude band, a maximum of semi-annual oscillation components seems to appear during the 2001 planet-encircling dust storm.

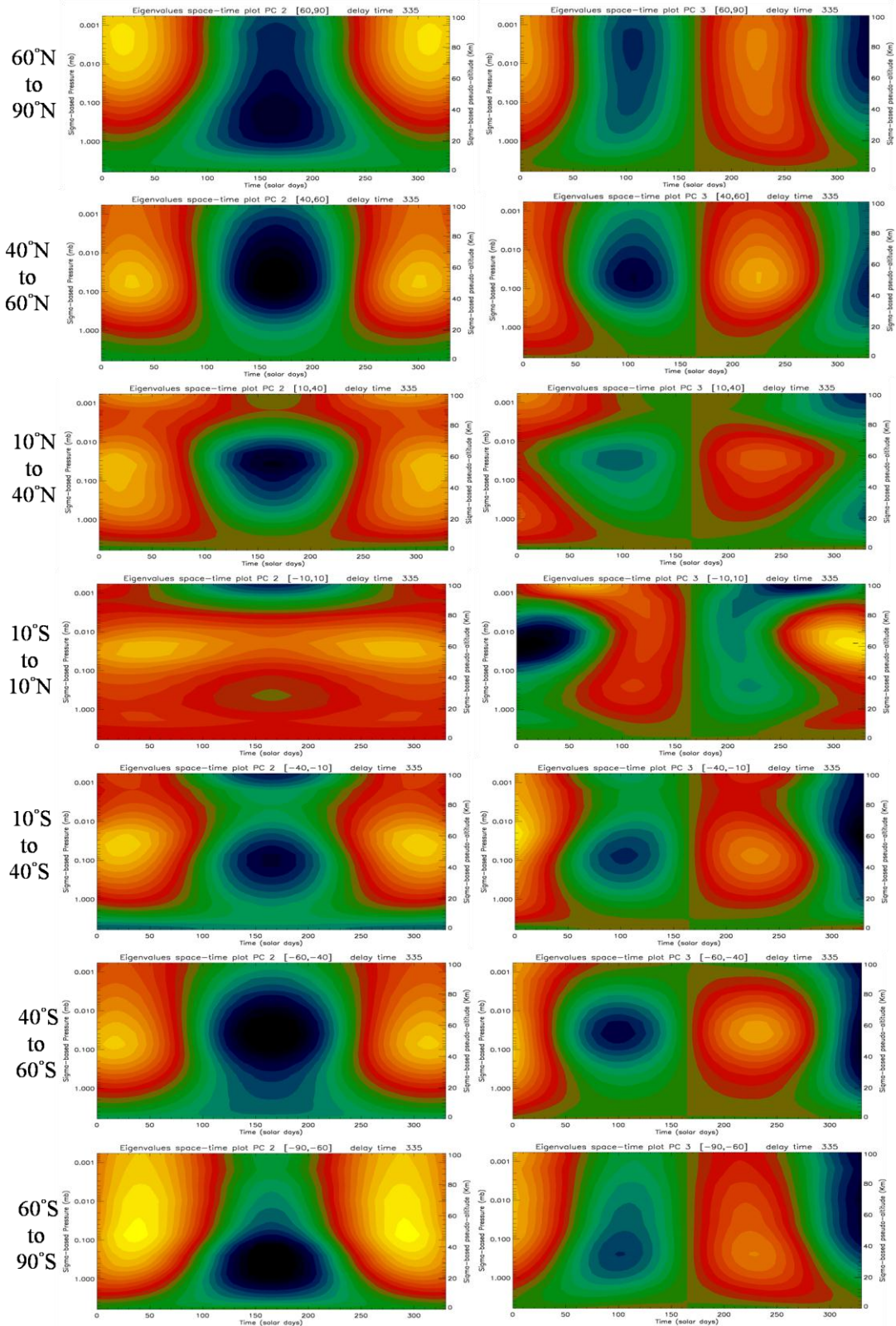


Figure 3.4. the third eigenvector height-time contour (left column) and the fourth eigenvector height-time contour (right column). From the toppest row to the lowest row, the results are presented in order of 60°N and 90°N, 40°N and 60°N, 10°N and 40°N, 10°S and 10°N, 10°S and 40°S, 40°S and 60°S, 60°S and 90°S.

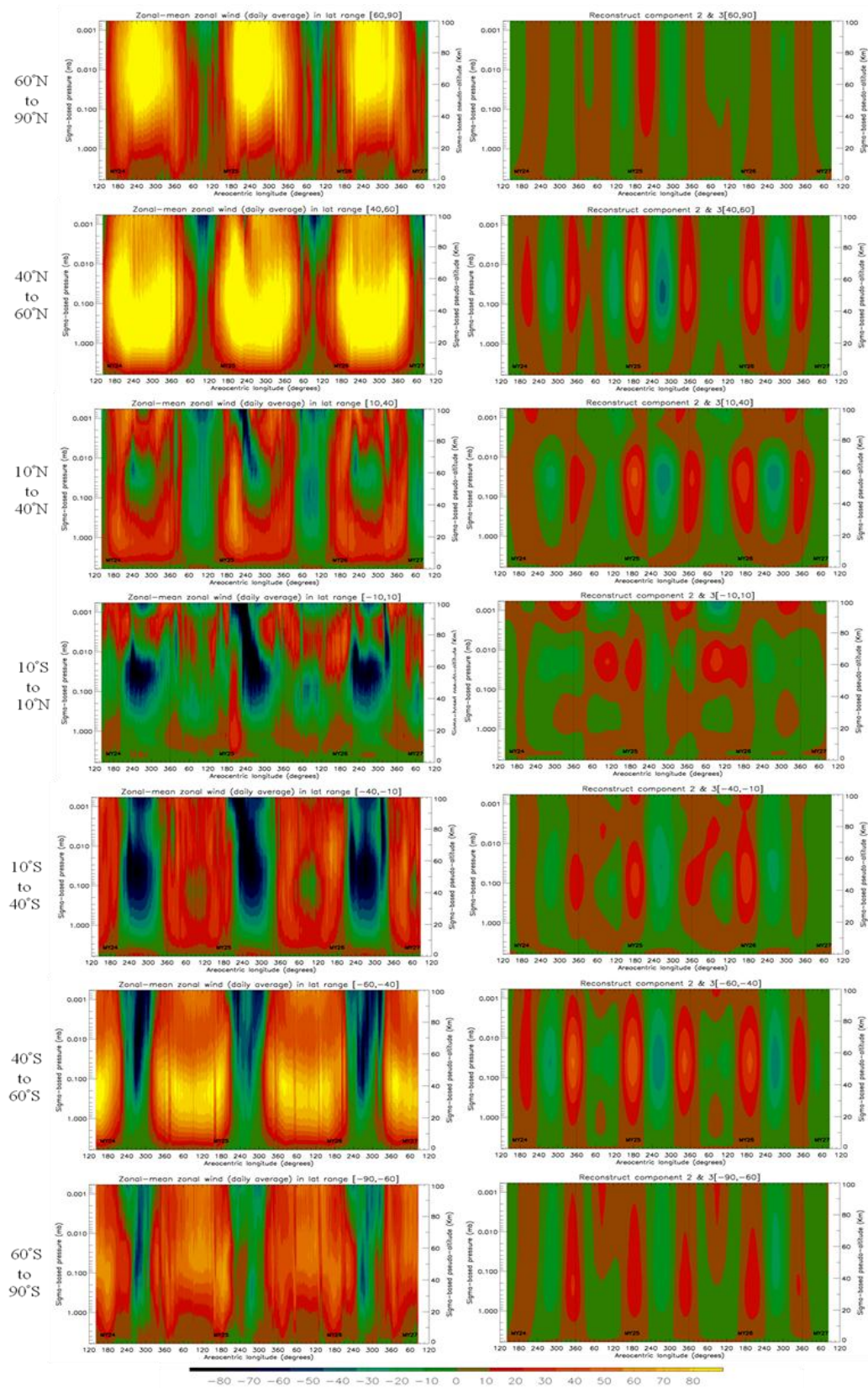


Figure 3.5. The raw zonal-mean of daily-averaged zonal wind in different latitude bands (left) and the reconstruction of the third and fourth PCs in the SSA analysis, which are corresponding to the semi-annual oscillation component.

Chapter 4 2-D Data Assimilation of Column Dust Opacity with Dust Transport

4.1 Background of the application of data assimilation on Mars

In the work of Montabone et al. [2005], Lewis et al. [2007] and the results shown in Chapter 3 of this report, the data assimilation results are all based on the data assimilation of column dust opacity without dust transport. The most important reason for excluding the dust transport feature in the MGCM has been the absence of observation for the dust vertical profiles [Montabone et al., 2005]. Thus the MGCM did not activate the dust transport scheme while conducting the data assimilation. The main integration loops for the current setting of the MGCM with data assimilation is shown in Figure 4.1. In the physics module the dust is distributed vertically in terms of an empirical relation (see Chapter 2), and the radiation is calculated using the dust opacity at each model level. Afterwards, the data assimilation scheme (AC) adjusts the temperature based on the observed temperature profiles followed by adjustment of the wind fields consistent with thermal wind balance. Finally, AC adjusts the column dust opacity at the reference level (*tauref*). Thus, these corrected variables become the input for next integration step.

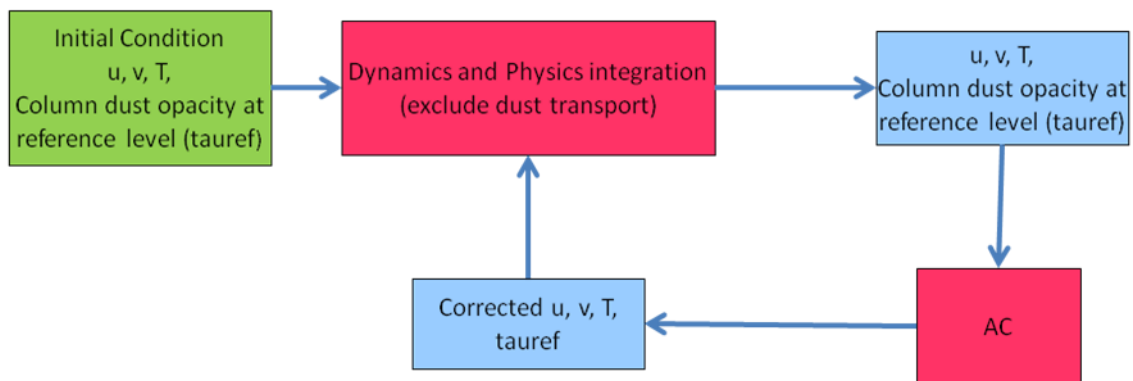


Figure 4.1. Illustration of the main calculation of atmospheric properties in current model setting, green box means the values from initial condition, blue box means data generated by MGCM integration and red box means the MGCM modules. (only the variables related to data assimilation scheme (AC) are included).

Given the normal operation of the MCS/MRO instrument, vertical information on the dust distribution has become newly available and has already been used for several published studies [McCleese et al., 2008; Kleinbohl et al., 2009; McCleese et

al., 2010]. As a result, it also provides the possibility of conducting 3-D dust assimilation with dust transport feature activated in the MGCM. Once this is implemented in the MGCM, it can make full use of the retrievals of dust profiles to obtain a more detailed understanding of the Martian atmosphere both in the weather aspects and the climatology. This chapter will present the recent progress of the first attempt to implement this more advanced data assimilation scheme by combining the 2-D dust data assimilation and dust transport scheme including dust lifting mechanisms (hereafter, dust transport scheme). Full 3-D dust assimilation will remain the ultimate future objective.

4.2 Approach of 2-D dust data assimilation with dust transport

Figure 4.2 illustrates the flow of the integration in the newly developed 2-D dust data assimilation with dust transport (hereafter, named *trans_AC*). The AC related variables u , v and T (only variables related to data assimilation are mentioned here.) will be integrated through the model dynamics module then used as inputs for integrating the physics and dust transport schemes respectively. Because the calculation of dust transport is based on the dust mass mixing ratio instead of dust opacity, the field of mass mixing ratio is also included in the initial condition. After that, the variables u , v , T and $tauref$ will go through the physics schemes and AC to obtain the corrected u , v , T and $tauref$. The major difference between the old version of the data assimilation and *trans_AC* is that one dust scaling factor is defined to propagate the corrected dust information into the vertical direction. The scaling factor is equal to the ratio of the corrected $tauref$ to the uncorrected $tauref$ at a particular time step. Because we only assimilates column dust opacity $tauref$ in this version of data assimilation, a strong assumption has been made that the percentage change due to the correction of $tauref$ (scaling factor defined above) should be the same for the change of aerosol opacity in any vertical layer ($aerosol(L)$).

Because the dust opacity regarding of layer thickness at each layer ($aerosol(L)$) can be calculated by,

$$aerosol(L) = \int_{p_{L+1}}^{p_L} q_{extrhor} * q(L) * \frac{dp}{g}$$

where,

$$q_{extrhor} = \frac{3}{4} * \frac{Q_{ext}}{\rho * radius}$$

L : level index

p : pressure at particular level

q : dust mass mixing ratio
 g : gravitational acceleration on Mars
 Q_{ext} : extinction coefficient
 ρ : dust density
radius : stand for radius of dust particle

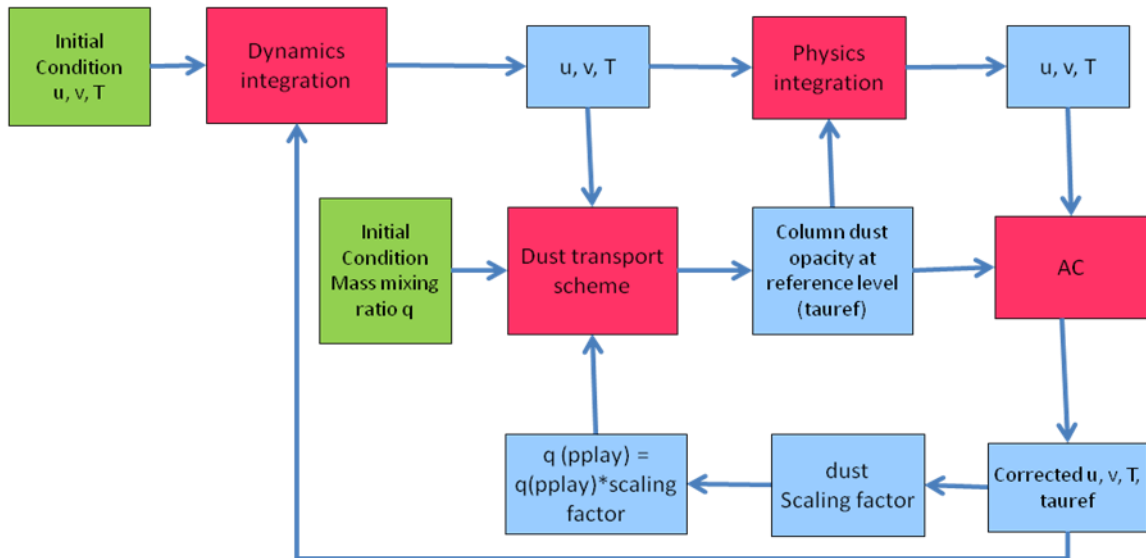


Figure 4.2. Illustration of the main calculation of atmospheric properties in the newly developed scheme, green box means the values from initial condition, blue box means data generated by MGCM integration and red box means the MGCM modules. (only the variables related to data assimilation scheme (AC) are included)

Meanwhile, the column dust opacity can be obtained by simply summing up $aerosol(L)$ in the vertical direction. At a particular integration time step, the extinction coefficient and layer thickness should be constant for particular model grid at certain layer. As a result, the scaling factor can be applied directly to multiply dust mass mixing ratio q to perform the correction.

4.3 Preliminary results

The preliminary results present in this chapter are for only 30 days simulation, starting from Martian day 331 to day 361 in MY 24. They all start from the same initial condition, although the initial condition may not be perfect (e.g. only 60 days spin-up time). In each figure, the upper panel is from the free running MGCM with dust transport scheme activated (hereafter, *trans*), middle panel is from the existing data assimilation without dust transport (hereafter, *ACM*), while the bottom one is for

AC with dust transport, denoted as *trans_AC*.

In order to easily understand the results produced by this new approach, only one dust particle size bin is chosen for this preliminary study of MGCM column dust data assimilation with dust transport, although multi-size dust transport and the capability of predicting the distribution of dust particle sizes is also included in the MGCM. The possibility of conducting data assimilation with multi-size dust transport could be investigated in future work beyond this project. In addition, other dust transport related mechanisms (radiatively active dust, dust lifting by wind stress, dust lifting by dust devil and sedimentation) remain functional.

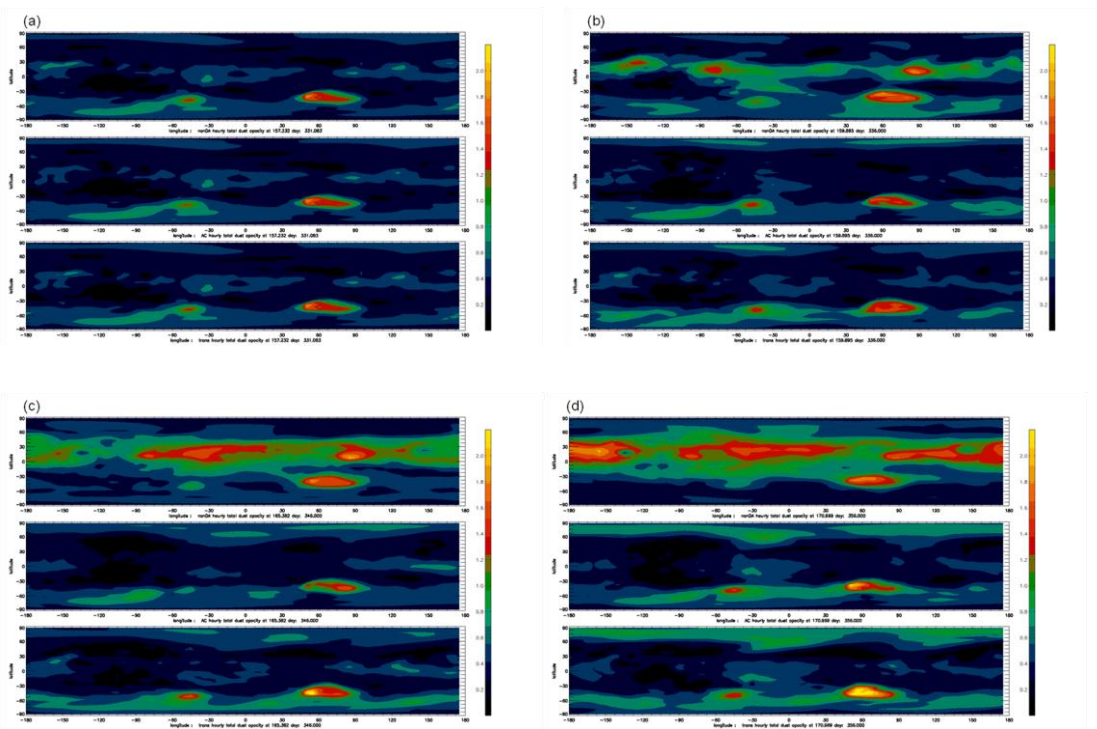


Figure 4.3. column dust opacity simulated by MGCM, in each figure, upper panel is for trans scenario, middle panel is for ACM scenario and lower panel is for trans_AC scenario (new approach), (a) the first two-hour simulation, (b) simulation results after 5 days from initial, (c) simulation results after 15 days from initial, (d) simulation results after 25 days from initial.

The simulation results for three scenarios are shown in Figure 4.3. The results are output every two hours during the simulation, and after the first two hours (Figure 4.3a), the nearly similar patterns (high column dust opacity on Hellas) coming from initial conditions can still be observed at this early simulation time. After 5 days integration, the dust starts to accumulate on the equator, and at low and middle

latitudes in the *trans* scenario (upper panel in Figure 4.3b). It is noticeable that in the *trans* scenario more dust spreads into the northern hemisphere compared to the southern hemisphere, and three regions of high column dust opacity develop in the northern hemisphere. For the *ACM* (middle panel in Figure 4.3b) and *trans_AC* (lower panel in Figure 4.3b) cases, the patterns for the dust distribution are quite similar to each other, except that in high southern latitudes, a dust transport path can be observed between two areas of high column dust opacity. 15 days from initialization (Figure 4.3c), the dust continues to accumulate in the northern hemisphere in *trans* (upper panel in figure 4.3c), and the column dust opacity is higher in both high value areas of the southern hemisphere in *trans_AC* than those in *ACM* (location around (-45°S, -45° in longitude), (-45°S, 60° in longitude)). Moreover, areas with column dust opacity higher than 0.8 cover most of the south polar area in *trans_AC*. In the day 25 of *trans*, plenty of dust have formed a band with high column dust opacity in the middle latitudes of northern hemisphere (30°N). The main difference between *ACM* and *trans_AC* is the higher column dust opacity in the dust-rich area of southern hemisphere ((-45°S, 60° in longitude)). Overall, the results of *ACM* and *trans_AC* are

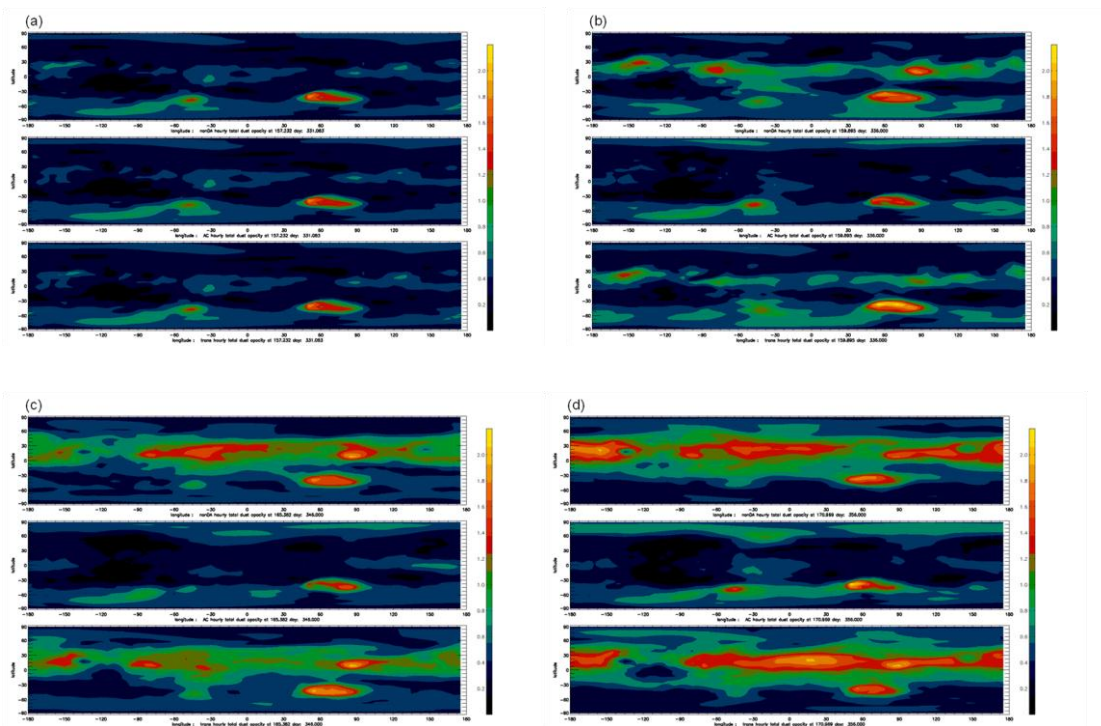


Figure 4.4. column dust opacity simulated by MGCM without observation constraint after 2 days, in each figure, upper panel is for *trans* scenario, middle panel is for *ACM* scenario and lower panel is for *trans_AC* scenario (new approach), (a) the first two-hour simulation, (b) simulation results after 5 days from initial, (c) simulation results after 15 days from initial, (d) simulation results after 25 days from initial.

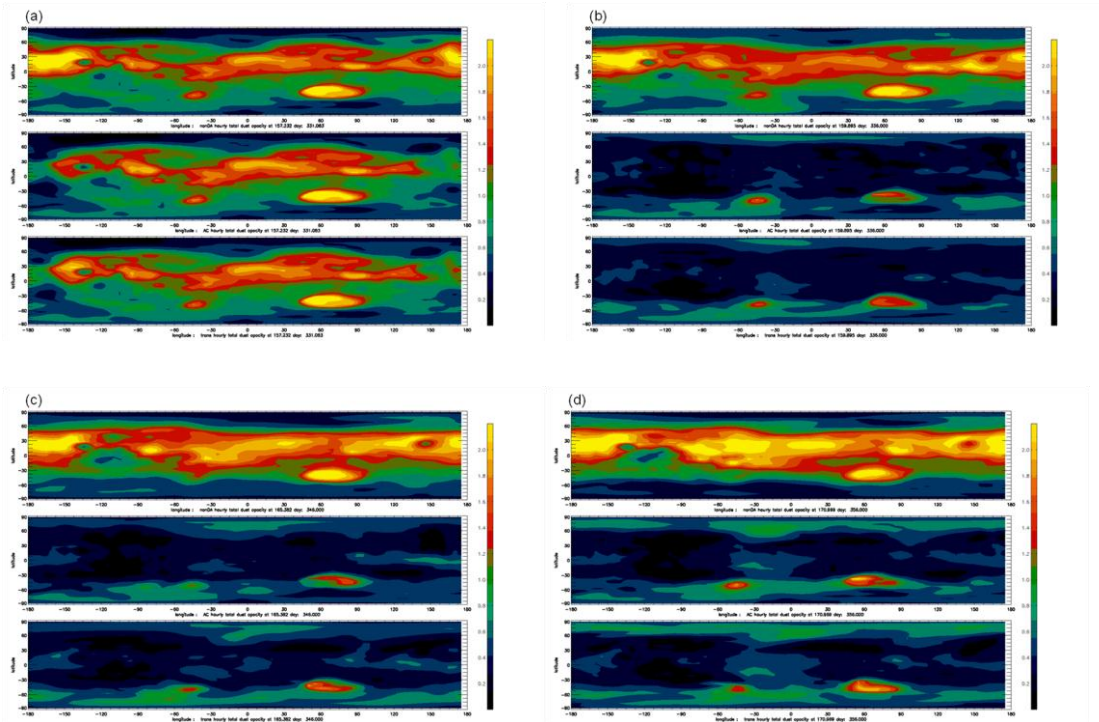


Figure 4.5. column dust opacity simulated by MGCM with extremely high initial conditions of column dust opacity, in each figure, upper panel is for trans scenario, middle panel is for ACM scenario and lower panel is for trans_AC scenario (new approach), (a) the first two-hour simulation, (b) simulation results after 5 days from initial, (c) simulation results after 15 days from initial, (d) simulation results after 25 days from initial.

constrained quite well by the data assimilation technique. A relatively clear path of dust transport in the high latitudes of the southern hemisphere can be seen in *trans_AC*, and this is a new feature which can not be represented in *ACM* as the dust remains static in that case.

In order to further understand the effect of the new data assimilation approach (*trans_AC*), two experiments were designed. One will runs the MGCM as a free-running GCM after assimilating two days of observations in *trans_AC* (Figure 4.4), and the other one employs a dust distribution with extremely high column dust opacity as an initial condition for all three scenarios (*trans*, *ACM* and *tran_AC*; see results in Figure 4.5).

In Figure 4.4, after the first two hours of simulation (Figure 4.4a), all three scenarios have almost the same pattern for column dust opacity. 5 days later (Figure 4.4b), when the dust starts to accumulate in the low and middle latitudes in *trans*

(upper panel in Figure 4.4b), some dusts also start to accumulate in low latitudes in *trans_AC* (lower panel in Figure 4.4b), and for the areas with high column dust opacity of southern hemisphere, the one near (-45°S, -45° in longitude) appears to dissipate, and the one near (-45°S, 60° in longitude) has highest value than those in the other scenarios. 15 days from initial (Figure 4.4c), *trans_AC* has formed similar pattern of column dust opacity to that in *trans*, but with smaller coverage of column dust opacity higher than 1.2. In day 25 (Figure 4.4d), the values of column dust opacity in northern hemisphere look indicate more dusts accumulate in *trans_AC* than that in *trans*.

Figure 4.5 shows the experiment with an extremely high initial condition of column dust opacity. Extremely high column dust opacity can still be seen in Figure 4.5a after the first two hours from starting the simulation. However, in day 5 (Figure 4.5), the redundant dusts in the *ACM* (middle panel in Figure 4.5b) and *trans_AC* (lower panel in Figure 4.5b) have been “removed” by the data assimilation scheme, and the patterns became similar to the corresponding plots in Figure 4.3. Evolving with time, the high column dust opacity in the *trans* simulation indicates the redundant dust can not be “removed” at the finish of whole 30-day simulation by the dust sedimentation scheme in MGCM, but the data assimilation scenarios (*ACM* and *trans_AC*) eventually converge back to the results shown in Figure 4.3.

Chapter 5 Conclusions and Future Plans

5.1 Conclusions

This report presents the works which has been done in my first year enrolled in the DPhil program in Atmospheric, Oceanic and Planetary Physics (AOPP) of the University of Oxford. A Martian General Circulation Model (MGCM), developed mainly in UK (University of Oxford and The Open University) with joint efforts of Laboratoire de Météorologie Dynamique (LMD; Paris, France) and Instituto de Astrofísica de Andalucía (Granada, Spain), is employed in this DPhil project to make use of the newly available vertically resolved dust opacity data from MCS. In terms of that particular purpose, a more advanced data assimilation technique has to be developed. The current data assimilation scheme in MGCM only assimilates the temperature profiles and column dust opacity at a reference level (*tauref*), and the dust would not be transported in the light of model predicted variables. In terms of technical aspects, our aim is to develop a new data assimilation scheme which is able to assimilate the profiles of dust opacity to correct the dust fields predicted by the MGCM dust transport scheme. Based on this new data assimilation technique and available observations, a complete and dynamically self-consistent reconstruction of the entire global circulation will be made. Such a record will then be used for a series of diagnostic studies to characterize the detailed climatology and synoptic meteorology of Mars over seasonal and interannual timescales. This can include detailed case studies of events such as the formation of cyclonic weather systems and initiation of regional dust storms.

The work of analyzing the semi-annual oscillation from the assimilated results produced by Montabone et al. [2005] has been presented not only in the Chapter 3 of this report, but also in the Fourth International workshop on the Mars Atmosphere: modeling and observations held in Paris, France in February of 2011. We analyzed the raw zonal-mean of daily-averaged zonal wind to obtain survey of the semi-annual oscillation in the Martian atmosphere and its structure in the different latitude bands (see Figure 3.2). Afterwards, the details of the Martian semi-annual oscillation were unveiled on the basis of Singular Spectrum Analysis (SSA). The second largest pair of Principal Components (PCs) represents the semi-annual oscillation, and their corresponding eigenvectors show that a coherent semi-annual signal can be observed in most altitudes outside the Planetary Boundary Layer (PBL), especially outside the equator. The reconstructions of the third and fourth PCs indicate the semi-annual

oscillation can be amplified by the annual oscillation signal. On extending the view to the polar regions, the semi-annual oscillation becomes more significant, but the overall amplitude reaches its maximum in the middle latitude bands (40°N and 60°N, 40°S and 60°S) in both hemispheres. This phenomenon can not be seen clearly in the raw zonal-mean of daily-averaged zonal wind, since the amplitude of annual oscillation is too strong and obscures this feature. However, in the low latitudes of northern hemisphere (10°N and 40°N) and equator (10°S and 10°N), the cause of the interesting abrupt changes of fifth PC amplitude during the 2001 planet-encircling dust storm (MY 25) is still under investigation.

The progress of developing data assimilation scheme with dust transport was addressed in Chapter 4 of this report. Our first attempt was to assimilate the observed *tauref* to further correct the predicted dust mixing ratio based on the assumption that the percentage change due to the correction of *tauref* should be the same in any vertical layer. This approach actually propagates the 2-D dust information into the vertical on the basis of an assumption that the scaling factor defined above is the same for particular model grid at particular time step in different layers. The preliminary results seem to be reasonable and encouraging. While showing the dust transport path predicted by the dust transport scheme, the new data assimilation approach presented in this report can still remove excess dust when required by the observations, making the final simulation converge to the simulation produced by the old assimilation scheme. Certainly, further investigations still need to be done to validate this method, and to provide the useful experience to the assimilation of dust opacity profiles with dust transport.

5.2 Future Work

For the study of the Martian semi-annual oscillation, the next step is to investigate the possible trigger and related effect of abrupt changes of fifth PC in the low latitude of northern hemisphere (10°N and 40°N) and equator (10°S and 10°N). So far, the triggers of dust events especially the global dust storms on Mars have not yet been found out. It is interesting that this abrupt change of fifth PC from the SSA of zonal-mean zonal wind happens more or less at the time of the start of 2001 planet-encircling dust storm (MY 25). Thus, to question if this abrupt change is a side-effect of the global dust storm or if this is the trigger of the global dust storm can be an interesting topic to look into, and probably lead this study to completion in January of year 2012. In the coming three months, the possible correlation between the phase change of the semi-diurnal tide and the abrupt amplitude change of

zonal-mean zonal wind will be analyzed, as well as the correlation with dust opacity itself. In the work of Kuroda et al. [2008], they used the horizontal momentum equation in the Transformed Eulerian Mean (TEM) formalism [Andrews et al., 1987],

$$\frac{\partial \bar{u}}{\partial t} = \bar{v}^* \left[f - \frac{(\bar{u} \cos \phi)_\phi}{a \cos \phi} \right] - \bar{w}^* \bar{u}_z + \frac{\nabla \cdot F}{\rho_0 a \cos \phi} + \bar{X}$$

where \bar{u} is the mean zonal wind, $(0, \bar{v}^*, \bar{w}^*)$ is the residual mean meridional circulation, overbars denote zonal averaging, f is the Coriolis parameter, a is the radius of Mars, ϕ is the latitude, F is the Eliassen-Palm (EP) flux due to non-zonal eddies, ρ_0 is the atmospheric reference density, and \bar{X} is the parameterized (subgrid) forcing. In their study, they claim that on the equator the vertical advection and the diurnal sun-synchronous tide are the main drivers of the prograde phase of the SAO during equinoxes. It is meaningful to examine this explanation in our assimilation results presented in Chapter 3. Furthermore, we can extend this investigation outside the equator. In the right hand side of above equation, the first two terms are relatively easy to calculate. However, as the UK MGCM is based on a spectral solver, the actual vertical velocity has to be obtained by solving the Omega equation before calculating the third term $\bar{w}^* \bar{u}_z$. And most time will be spent on working out the fourth terms.

As the main objective of this DPhil project is to make use of newly available datasets from the Mars Climate Sounder instrument on board NASA's Mars Reconnaissance Orbiter, before going into the 3-D data assimilation of dust opacity profiles, the 2-D data assimilation scheme with dust transport introduced in Chapter 4 of this report needs to be further validated. However, datasets from the on-board Thermal Emission Spectrometer (TES) of Mars Global Surveyor (MGS) do not provide the dust profile observations to compare with the model assimilated dust vertical distribution. One alternative is to convert the sequential MCS dust profiles to total column dust opacity, and then assimilate this column dust opacity dataset. Eventually, we can retrieve the vertical dust profiles simulated by 2-D data assimilation scheme with dust transport to make a comparison with the original MCS dust profiles. Although lack of the observation of dust opacity in low Martian atmosphere as a result of the difficulty brought in by the weak contrast between Martian surface and low atmosphere, this method is probably the best-available approach to validate this new data assimilation technique. After finishing the validation of 2-D dust data assimilation scheme with dust transport, it can be used to produce a record of Martian atmosphere by assimilating the TES temperature profiles and dust column opacity. Such a record can be very useful to initially unveil the vertical information of dust and the temperature adjustment as a result of the radiation

effect of dust particles.

Ultimately, the new dust data assimilation scheme with dust transport should be capable of assimilating dust profiles from MCS datasets while simultaneously transporting the dust. The data assimilation approach of temperature profiles in the MGCM has been described in Chapter 2. The temperature fields in MGCM are averaged in terms of the altitudes of temperature retrievals. Thus, the model increments of the averaged temperature fields are determined by assimilating the temperature profiles from instruments. The similar approach will be applied to 3-D dust data assimilation. The dust is transported in terms of the predicted wind fields and temperature, and then before distributing the model increments to each model layer the dust fields will be corrected by the incoming observation profiles in the light of averaged model layers. At least before the start of this project, no other solid publication of 3-D dust data assimilation on Mars had become available. Once the technical implementation and validation is completed, it is possible to produce a several-year record to diagnose the climatology on Mars in terms of atmospheric properties mainly focusing on dust-related features. We can extend the investigation of interannual and interseasonal variability of Martian dust in 3-D aspect, and such a record is also useful to document the spacial and vertical evolution of individual regional dust storms on the basis of this four-dimensional best-fit to the observation.

5.3 Expected Timetable

The future works of this DPhil project are expected to be done in the timetable shown in Figure 5.1.

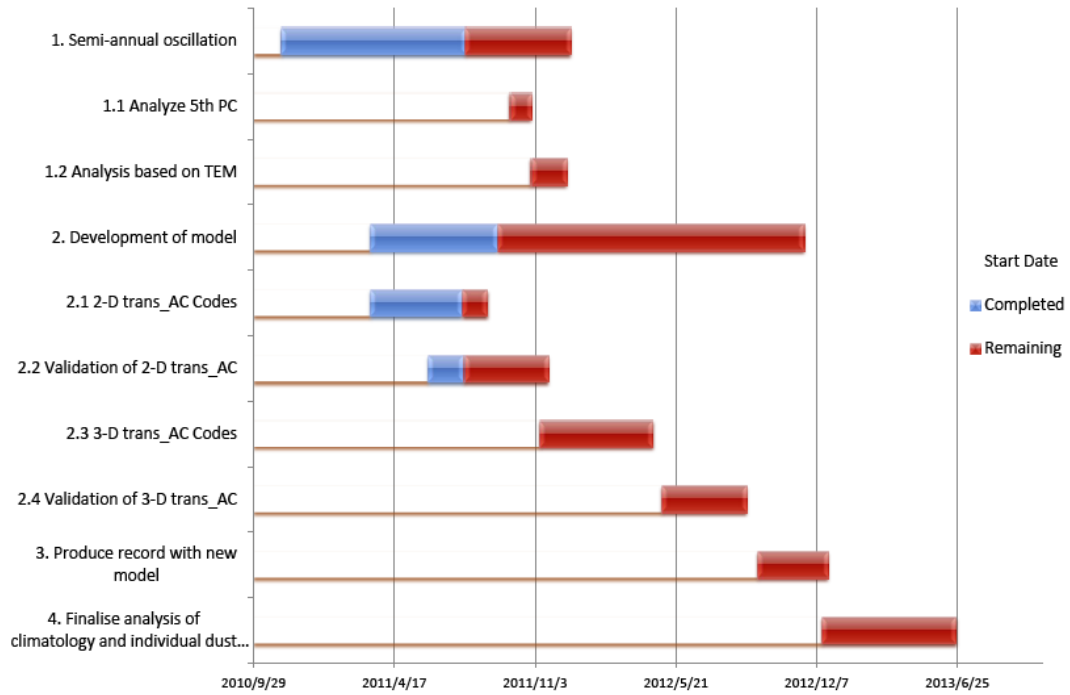


Figure 5.1. Expected timetable for the future works of DPhil project.

Bibliography

Basu, S., M. I. Richardson and R. J. Wilson (2004), Simulation of the Martian dust cycle with the GFDL Mars GCM, *J. Geophys. Res.* *109*(E11006), doi: 10.1029/2004JE002243.

Benson J. L., D. M. Kass and MCS Team (2011), Mars Climate Sounder observations of ice and dust layering in the Martian atmosphere, Fourth International Workshop on Mars Atmosphere Modeling and Observations, Paris, France, Feb. 2011.

Cantor, B. A., P. B. James, M. Caplinger, and M. J. Wolff, Martian dust storms: 1999 Mars Orbiter Camera observations. *J. Geophys. Res.* *106*, 23, 653-23,687, 2001.

Collins, M., S. R. Lewis, P. L. Read and F. Hourdin (1996), Baroclinic wave transitions in the Martian atmosphere, *Icarus*, *120*, 344-357.

Conrath, B. J. (1975), Thermal structure of the Martian atmosphere during the dissipation of dust storm of 1971, *Icarus*, *24*, 36-46, 1975.

Conrath, B. J., J. C. Pearl, M. D. Smith, W. C. Maguire, S. Dason, M. S. Kaelbere and P. R. Christensen (2000), Mars Global Surveyor Thermal Emission Spectrometer (TES) observations: atmospheric temperatures during aerobraking and science phasing, *J. Geophys. Res.* *105*, 9509-9520.

Euler, E. A., S. D. Jolly and H. H. 'Lad' Curtis (2001), The failures of the Mars Climate Orbiter and Mars Polar Lander: a perspective from the people involved, 24th annual AAS guidance and control conference, January 31-February 4, 2001, Breckenridge, Colorado, USA.

Fenton, L. K., and M. I. Richardson (2001), Martian surface winds: Insensitivity to orbital changes and implications for aeolian processes, *J. Geophys. Res.*, *106*, 32,885– 32,902

Forget, F., F. Hourdin, R. Fournier, C. Hourdin, O. Talagrand, M. Collins, S. R. Lewis, P. L. Read and J.-P. Huot (1999), Improved general circulation models of the martian atmosphere from the surface to above 80 km, *J. Geophys. Res.* *104* (E10), 24155-24176.

Garcia, R. R., T. J. Dunkerton, R. S. Lieberman and R. A. Vincent (1997), Climatology of the semiannual oscillation of the tropical middle atmosphere, *J. Geophys. Res.*, *102*,

26019-26032.

Ghil, M. and K. Mo (1990), Intraseasonal oscillations in the global atmosphere. Part II: Southern Hemisphere, *J. Atmos. Sci.*, *48*(5), 780-790.

Hamilton, K. (1995), Interannual variability in the northern hemisphere winter middle atmosphere in control and perturbed experiments with the GFDL SKYHI general circulation model, *J. Atmos. Sci.*, *52*, 44–66.

Hoskins, B. J. and A. J. Simmons (1975), A multi-layer spectral model and the semi-implicit method, *Q. J. R. Meteorol. Soc.*, *101*, 637-655.

Hourdin, F., F. Forget, and O. Talagrand (1995), The sensitivity of the Martian surface pressure and atmospheric mass budget to various parameters: A comparison between numerical simulations and Viking observations, *J. Geophys. Res.*, *100*(E3), 5501–5523, doi:10.1029/94JE03079.

Kahre, M. A. and R. M. Haberle (2010), Mars CO₂ cycle: Effects of airborne dust and polar cap ice emissivity, *Icarus*, *201*, 648-653.

Kuroda, T., A. S. Medvedev, P. Hartogh and M. Takahashi (2008), Semiannual oscillations in the atmosphere of Mars, *Geophys. Res. Lett.*, *35*, L23202, doi:10.1029/2008GL036061.

Lee, C., et al. (2009), Thermal tides in the Martian middle atmosphere as seen by the Mars Climate Sounder, *J. Geophys. Res.*, *114*, E03005, doi:10.1029/2008JE003285.

Lewis, S. R. and P. R. Barker (2005), Atmospheric tides in a Mars general circulation model with data assimilation, *Adv. Space Res.* *36*(11), 2162-2168.

Lewis, S. R., P. L. Read, B. J. Conrath, J. C. Pearl and M. D. Smith (2007), Assimilation of thermal emission spectrometer atmospheric data during the Mars Global Surveyor aerobraking period, *Icarus* *192*, 327-347.

Lorenc, A. C., R. S. Bell and B. Macpherson (1991), The meteorological office analysis correction data assimilation scheme, *Q. J. R. Meteor. Soc.*, *117*, 59-89.

Mellor, G. L. and T. Yamada (1982), Development of a turbulence closure model for geophysical fluid problems, *Rev. of Geophys.*, *20*, 851-875.

- McCleese, D. J., et al. (2008), Intense polar temperature inversion in the middle atmosphere on Mars, *Nat. Geosci.*, *1*, 745–749, doi:10.1038/ngeo332.
- McCleese, D. J., et al. (2010), Structure and dynamics of the Martian lower and middle atmosphere as observed by the Mars Climate Sounder: Seasonal variations in zonal mean temperature, dust, and water ice aerosols, *J. Geophys. Res.*, *115*, E12016, doi:10.1029/2010JE003677.
- Montabone, L., S. R. Lewis and P. L. Read (2005), Interannual variability of martian dust storm in assimilation of several years of Mars Global Surveyor observations, *Adv. Space Res.* *36 (11)*, 2146-2155.
- Montabone, L., S. R. Lewis, P. L. Read and D. P. Hinson (2006a), Validation of martian meteorological data assimilation for MGS/TES using radio occultation measurements, *Icarus* *185 (1)*, 113-132.
- Montabone, L., S. R. Lewis and P. Withers (2006b), Reconstructing the weather on Mars at the time of the MERs and Beagle 2 landings, *Geophys. Res. Lett.*, *33*, L19202.
- Montabone, L., E. Millour and F. Forget (2010), WP 1.6 deliverable : Report on the analysis of available atmospheric observations at Exomars' phase B2X landing site, *Laboratoire de M'et'eorologie Dynamique, Universit'e "Pierre et Marie Curie", Paris, France*, March 31 2010.
- Murphy, J. R., J. B. Pollack, R. M. Haberle, C. B. Leovy, O. B. Toon, and J. Schaeffer (1995), Three-dimensional numerical simulation of Martian global dust storms, *J. Geophys. Res.*, *100(E12)*, 26,357–26,376, doi:10.1029/95JE02984.
- Newman, C. E., S. R. Lewis, P. L. Read and F. Forget (2002), Modeling the Martian dust cycle 1. Representations of dust transport processes, *J. Gerphys., Res.*, *107(E12)*, 5123, doi:10.1029/2002JE001910, 2002.
- Newman , C. E., S. R. Lewis, P. L. Read and F. Forget (2002), Modeling the Martian dust cycle, 2, Multiannual radiatively active dust transport simulations, *J. Gerphys., Res.*, *107(E12)*, 5124, doi:10.1029/2002JE001920, 2002.
- Pike, E. R., J. G. McWhirter, M. Bertero and C. deMol, (1984), Generalized information

theory for inverse problems in signal processing, *IEEE Proc.*, 131, 660-667.

Read, P. L. and S. R. Lewis (2004), *The Martian Climate Revisited: Atmosphere and Environment of a desert planet*, Praxis Publishing Ltd, Chichester, UK, 2004, printed in Germany.

Reed, J. R. (1966), Zonal wind behavior in the equatorial stratosphere and lower mesosphere, *J. Geophys. Res.*, 71, 4223-4233

Rennó, N. O., A. A. Nash, J. Lunine and J. Murphy (2000), Martian and terrestrial dust devils: test of a scaling theory using Pathfinder data, *J. Geophys. Res.*, 105(E1), 1859-1865.

Rogberg, P., P. L. Read, S. R. Lewis and L. Montabone (2010), Assessing atmospheric predictability on Mars using numerical weather prediction and data assimilation, *Q. J. R. Meteorol. Soc.*, 136, 1614-1635.

Schofield, J. T., D. M. Kass, A. Kleinböhl, D. J. McCleese, M. A. Allen, M. C. Foote, M. Jeganathan, F. Forget, A. Spiga, O. Talagrand, F. Lefèvre, A. Määttänen, T. Fouchet, N. Bowles, S. B. Calcutt, P. G. J. Irwin, P. L. Read, S. R. Lewis, J. R. Barnes, S. W. Bougher, R. M. Haberle (2011), *The Exomars Climate Sounder (EMCS) investigation*, Fourth International Workshop on Mars Atmosphere Modeling and Observations, Paris, France, Feb. 2011.

Smith, M. D. (2004), Interannual variability in TES atmospheric observations of Mars during 1999-2003, *Icarus*, 167, 148-165.

Sutton, J. L., C. B. Leovy and J. E. Tillman (1978), Diurnal variations of the Martian surface layer meteorological parameters during first 45 sols at two Viking lander sites, *J. Atmos. Sci.*, 35, 2346-2355.

Toon, O. B., J. B. Pollack and C. Sagan, Physical properties of the particles composing the Martian dust storm, *Icarus*, 30, 663-696, 1977.

Wilson, R. J., and K. Hamilton (1996), Comprehensive model simulations of thermal tides in the Martian atmosphere, *J. Atmos. Sci.*, 53, 1290-1326.

Wilson, R. J., S. R. Lewis, L. Montabone and M. D. Smith (2008), Influence of water ice clouds on Martian tropical atmospheric temperatures, *Geophys. Res. Lett.*, 35, L07202.